AGU ADVANCING EARTH AND SPACE SCIENCES

JGR Solid Earth

RESEARCH ARTICLE
10.1029/2023JB027474

Key Points:
- We propose a model to investigate the effect of multiscale cracks on seismic waves in tight sandstones
- The pore aspect ratio and crack-radius spectra are estimated at different differential pressures
- The permeability is obtained according to the pore geometry

Correspondence to:
L. Zhang,
zlin@hhu.edu.cn

Citation:
Ba, J., Zhu, H., Zhang, L., & Carcione, J. M. (2023). Effect of multiscale cracks on seismic wave propagation in tight sandstones. *Journal of Geophysical Research: Solid Earth*, *128*, e2023JB027474. https://doi.org/10.1029/2023JB027474

Received 15 JUL 2023
Accepted 5 OCT 2023

Author Contributions:
Conceptualization: Jing Ba, Lin Zhang, José M. Carcione
Data curation: Hesong Zhu, Lin Zhang
Formal analysis: Jing Ba, Hesong Zhu, Lin Zhang
Funding acquisition: Jing Ba, Lin Zhang
Investigation: Hesong Zhu, José M. Carcione
Methodology: Jing Ba, Hesong Zhu, Lin Zhang, José M. Carcione
Project Administration: Jing Ba
Software: Jing Ba, Hesong Zhu, Lin Zhang
Supervision: Jing Ba, Lin Zhang, José M. Carcione
Validation: Jing Ba, Hesong Zhu, Lin Zhang
Visualization: Lin Zhang
Writing – original draft: Jing Ba, Hesong Zhu, Lin Zhang
Writing – review & editing: Jing Ba, Lin Zhang, José M. Carcione

Effect of Multiscale Cracks on Seismic Wave Propagation in Tight Sandstones

Jing Ba[1], Hesong Zhu[1], Lin Zhang[1], and José M. Carcione[2]

[1]School of Earth Sciences and Engineering, Hohai University, Nanjing, China, [2]National Institute of Oceanography and Applied Geophysics – OGS, Trieste, Italy

Abstract Seismic wave propagation is affected by wave-induced local fluid flow between stiff pores and multiscale fractures. To investigate this phenomenon, forced vibration (1–100 Hz) and ultrasonic (10^6 Hz) measurements are performed on two tight sandstones with complex pore geometry in dry and water-saturated scenarios. Porosity, permeability, and ultrasonic velocities were also measured at different differential pressures. The results indicate that the nonlinear behavior of these properties is strongly influenced by the presence of cracks, and the correlations between the permeability/ultrasonic velocities and porosity are different. A wave propagation model is then developed in which penny-shaped cracks are inclusions introduced stepwise into a porous medium to describe the wave anelasticity in a wide frequency band at different pressures. As a result, the model provides good agreement with the measured P-wave velocity dispersion, and the pore aspect ratio spectrum and crack radii are determined. We then compare the estimated crack radii and pore size distributions from nuclear magnetic resonance spectroscopy. Published data of a tight sandstone and a low porosity sandstone in the frequency range (2–200, 10^6) and (1–3,000) Hz at different differential pressures are also analyzed to validate the model. The aspect ratios, volume fractions, and radii of pores/cracks are used to describe the measured permeability. The present work can provide new insights into the geophysical properties of reservoir rocks with complex pore geometry.

Plain Language Summary Multiscale cracks exert an important influence on the dispersion and attenuation of broadband acoustic waves. To better understand the underlying mechanism, we measured frequency-dependent elastic moduli and pressure-dependent porosity, permeability, and ultrasonic wave velocities of two tight sandstones. These data show that velocity dispersion is observable in water-saturated rock and that permeability and ultrasonic velocities are differentially correlated with porosity. A proposed wave propagation model, in which penny-shaped cracks are inclusions introduced stepwise into a porous medium, successfully describes the experimental data and other published data on tight sandstone and low-porosity sandstone, and aspect ratios, volume fractions, and radii of pores/cracks are determined.

1. Introduction

Subsurface rocks can be treated as cracked porous media. When seismic waves propagate through such rocks, different fluid pressures are generated at pores and multiscale cracks, implying different resonant frequencies and relaxation mechanisms (e.g., Ba et al., 2017; Borgomano et al., 2019; Carcione, 2022; Carcione & Picotti, 2006; Gurevich & Carcione, 2022; Guo & Gurevich, 2020; Müller et al., 2010; Sarout, 2012; Wei et al., 2021; Zhang et al., 2020, 2021). Therefore, for quantitative seismic interpretation to identify geofluids and characterize reservoirs and rocks, it is important to understand exactly how wave attenuation is affected by cracks.

Due to the complexity of the pore geometry, a double-porosity model is adopted to describe the rock's elastic response (e.g., Chapman et al., 2002; Dvorkin & Nur, 1993; Dvorkin et al., 1995; Gurevich et al., 2010; Mavko & Jizba, 1991; Mavko & Nur, 1975; Pride et al., 2004; Tang, 2011; Tang et al., 2012; Yao et al., 2015; Zhang, Ba, Carcione, et al., 2019). Crack density, aspect ratio, and radius are the main factors affecting the wave propagation. However, most of these works do not consider multiscale cracks.

The spatial distribution features of pores and cracks can be imaged with thin section tests (e.g., Peng & Johnson, 1972; Wawersik & Brace, 1971), scanning electron microscopy (SEM) (e.g., Arena et al., 2014; Burns et al., 1985; Griffiths et al., 2017; Hadley, 1976; Sprunt & Brace, 1974), and 3D X-ray CT (e.g., Sarout et al., 2017; Zhang & Toksöz, 2012). As stated in their works, the reliability of the result depends on the resolution of the imaging techniques. Another method is to use ultrasonic velocities measured at different differential

10.1029/2023JB027474

pressures (Cheng & Toksöz, 1979; David & Zimmerman, 2012; Deng et al., 2015; Duan et al., 2018; Izumotani & Onozuka, 2013; Tran et al., 2008; Zhang, Ba, Fu, et al., 2019; Zimmerman, 1990). However, the results may be non-unique. Moreover, pore geometry also affects the transport, electrical and thermal properties, which can also be utilized (e.g., Amalokwu & Falcon-Suarez, 2021; Han et al., 2016; Zhang et al., 2022).

For the case when fluid flow occurs between pores and cracks with different aspect ratios, Yan et al. (2014) modified and extended the elastic wave propagation theory with a single set of cracks proposed by Tang (2011), by utilizing a pore aspect ratio spectrum obtained from pressure-dependent ultrasonic velocities. Low-frequency measurements were not considered. Later, Tang et al. (2021) and Wang and Tang (2021) applied the estimated spectrum to describe the anelasticity at a wide range of frequencies, and their results are in agreement with those of forced oscillations (2–200 Hz) and ultrasonic (1 MHz) measurements at the different differential pressures. Sun and Gurevich. (2020) incorporated the spectrum into the squirt-flow model developed by Gurevich et al. (2010), and provided a reasonable description of the forced oscillation measurements. Other works were in recent years (e.g., Deng et al., 2015; Duan et al., 2018; Ouyang et al., 2021; Wu et al., 2022). However, the effect of crack radius on wave anelasticity has not been analyzed in these works.

To investigate the effect of multiscale cracks on the wave response, we measure porosity, permeability, and ultrasonic velocities at different differential pressures, and perform forced-oscillation measurements on core samples. Then, a theoretical model based on poroelasticity theory with a single set of penny-shaped cracks (Zhang, Ba, Carcione, et al., 2019) is proposed to interpret the measurements. Then, aspect ratios, volume fractions of pores and cracks, and crack radii are determined from the data. The estimated radii are compared with results from nuclear magnetic resonance (NMR) spectroscopy. Then, the model is applied to interpret laboratory measurements on a tight sandstone and a low-porosity sandstone.

2. Experiments

Two tight-sandstone samples (TS4 and TS5) with 25.3 and 25.29 mm in diameter and 60.1 and 56.76 mm in length were extracted from the Jurassic Shaximiao Formation of Sichuan Basin. The porosities (ϕ), permeabilities (κ), and dry-rock densities (ρ_{dry}) are 8.77% and 11.78%, 0.149 and 0.3985 mD, and 2.44 and 2.35 g/cm^3, respectively. According to a thin section analysis (Figure 1), the samples mainly consist of quartz, feldspar, clay, and calcite. Solid grains are subangular or subrounded, and compactly arranged with pore-contact cementations. Pores and cracks at different scales can be observed.

To investigate the effect of multiscale cracks on wave velocity dispersion and attenuation, the frequency-dependent Young's modulus (E) and Poisson's ratio (v) are measured by using a forced oscillation instrument (Figure 2a). More details on the device and data processing can be found in Sun et al. (2022) and Zhao et al. (2019). In the experiment of this study, the sample is first dried in an oven at 60°C for 12 hr and then humidified in a sealed dish for 2–3 days. Then, the specimen and two aluminum standards are glued together and axial stress oscillations generated by piezoelectric transducers (PZTs) are applied. The axial and radial strain amplitudes of the specimen and standards are recorded with strain gauges. The arrangement is shown in Figure 2b. Consequently, E and v are determined at seismic frequencies (1–100 Hz), at dry conditions, and at room temperature (~25°C). For the saturation method, the sample is first immersed in a water tank to allow spontaneous saturation. To achieve complete water saturation, the air is evacuated by suction, and then the water pressure is increased so that the water fills the pores/cracks. This process is repeated until there is no change in the weight of the sample. Saturation is determined by comparing the weight of the sample to that of the water. The water-saturated sample is then tested with the same instrument. Ultrasonic velocities are simultaneously measured at a center frequency of 1 MHz with transducers mounted on the top and bottom ends of the sample (Figure 2a). The pore (confining) pressure and vertical stress are set as 1 (1) atm and 5 MPa, respectively.

The experimental procedure of Zhang et al. (2022) is used to measure porosity, permeability, and ultrasonic wave velocities at different pressures, where the former two are measured at a constant pore pressure of 1.38 MPa and a confining pressures of 3.45–59.98 MPa by using a helium porosimeter permeameter (Figure 2c), and the velocities are measured at a constant pore pressure of 10 MPa and confining pressures of 12–60 MPa in nitrogen gas and water-saturated cases with an ultrasonic experimental setup (Figure 2d) in which PZTs have a center frequency of 0.5 MHz. In addition, NMR spectroscopy was performed to characterize the pore/crack size distribution. The pore fluids used in the experiments are nitrogen gas and water, whose density, bulk modulus, and viscosity are 112.6/1,000 kg/m^3, 0.0161/2.25 GPa, and 0.000017/0.001 Pa·s, respectively.

10.1029/2023JB027474

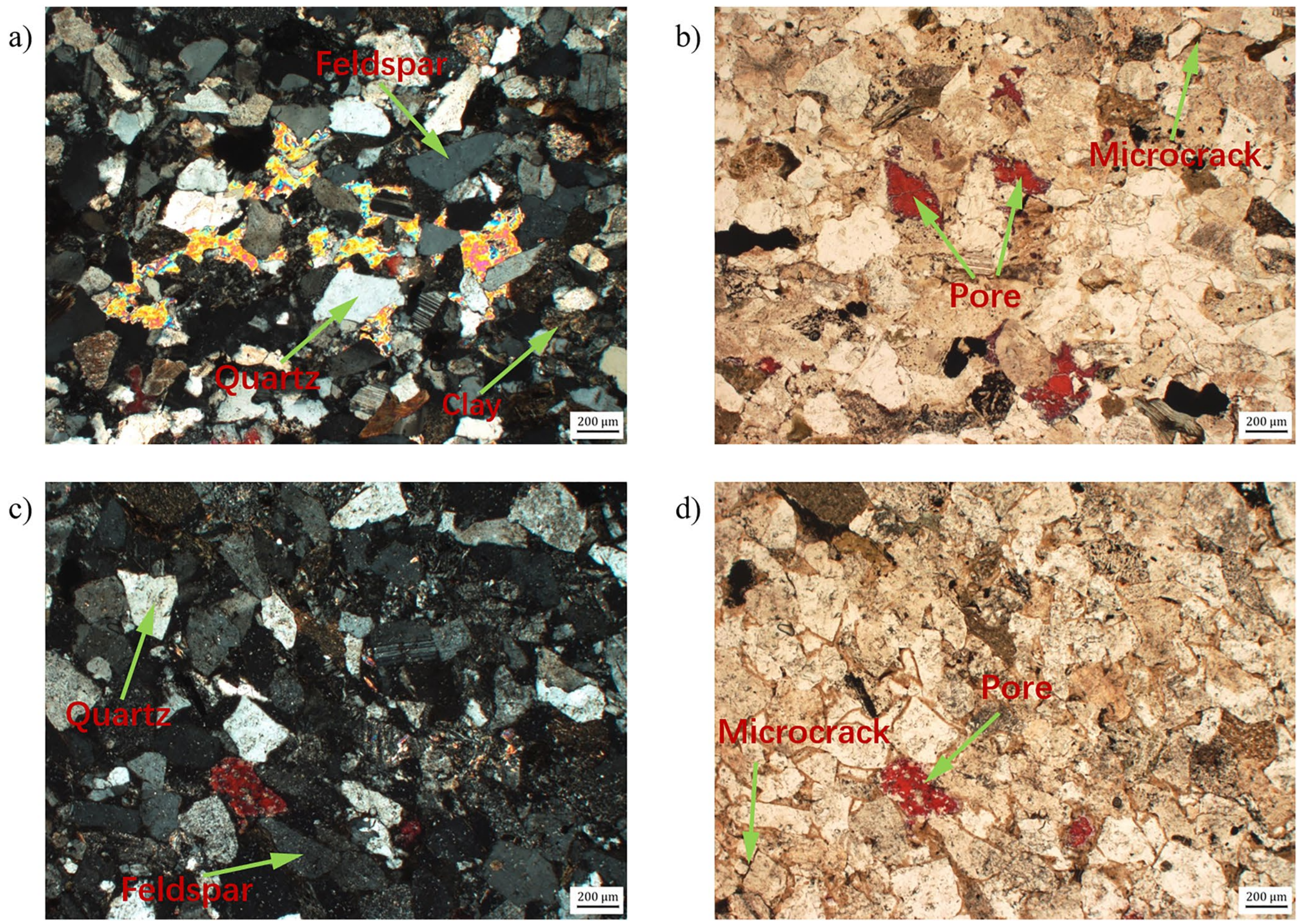

Figure 1. Thin sections of TS4 (a, b) and TS5 (c, d) samples, with orthogonal (left) and single (right) polarization images. The red color corresponds to the pore space.

3. Experimental Results

3.1. Permeability and Porosity

Figure 3 shows the relationship between permeability and porosity for the two samples. As expected, permeability increases (decreases) with increasing porosity (pressure) and shows a positive correlation with porosity, with a significant decrease in permeability in a high porosity range (i.e., low P_d) and then a gradual decrease to a low porosity (i.e., high P_d). This nonlinear property can be attributed to the presence of cracks (e.g., Walsh, 1965; Zimmerman, 1990). The relationship between porosity (permeability) and differential pressure can be expressed as a combination of linear and exponential terms (e.g., Shapiro, 2003; Shapiro et al., 2015). For TS4, $\phi = 7.55 - 0.00002P_d + 1.2e^{-0.11P_d}$ ($R^2 = 0.982$), $\kappa = 0.086 - 0.00025P_d + 0.077e^{-0.082P_d}$ ($R^2 = 0.962$). For TS5, $\phi = 9.65 - 0.00092P_d + 2.14e^{-0.165P_d}$ ($R^2 = 0.962$), $\kappa = 0.33 - 0.00042P_d + 0.096e^{-0.14P_d}$ ($R^2 = 0.993$). In these empirical relations, the first two and last terms correspond to changes of pore and crack porosities (permeabilities) with pressure, respectively.

3.2. Ultrasonic Velocities

By selecting the first arrivals of the waveforms in the discharge process, we obtain the P- (V_P) and S- (V_S) velocities in nitrogen gas and water-saturated cases. We resampled the porosity along the pressure stations used for the velocity measurements; the velocities versus porosity are shown in Figure 4. The velocities are also correlated with porosity, while the trend with porosity is basically inverse to permeability, that is, the velocities increase significantly at high porosity and then the rate of variation decreases gradually at low porosity. It is also observed that the P-wave velocity in a water-saturated case is higher than in a nitrogen gas case, while the S-wave velocity

10.1029/2023JB027474

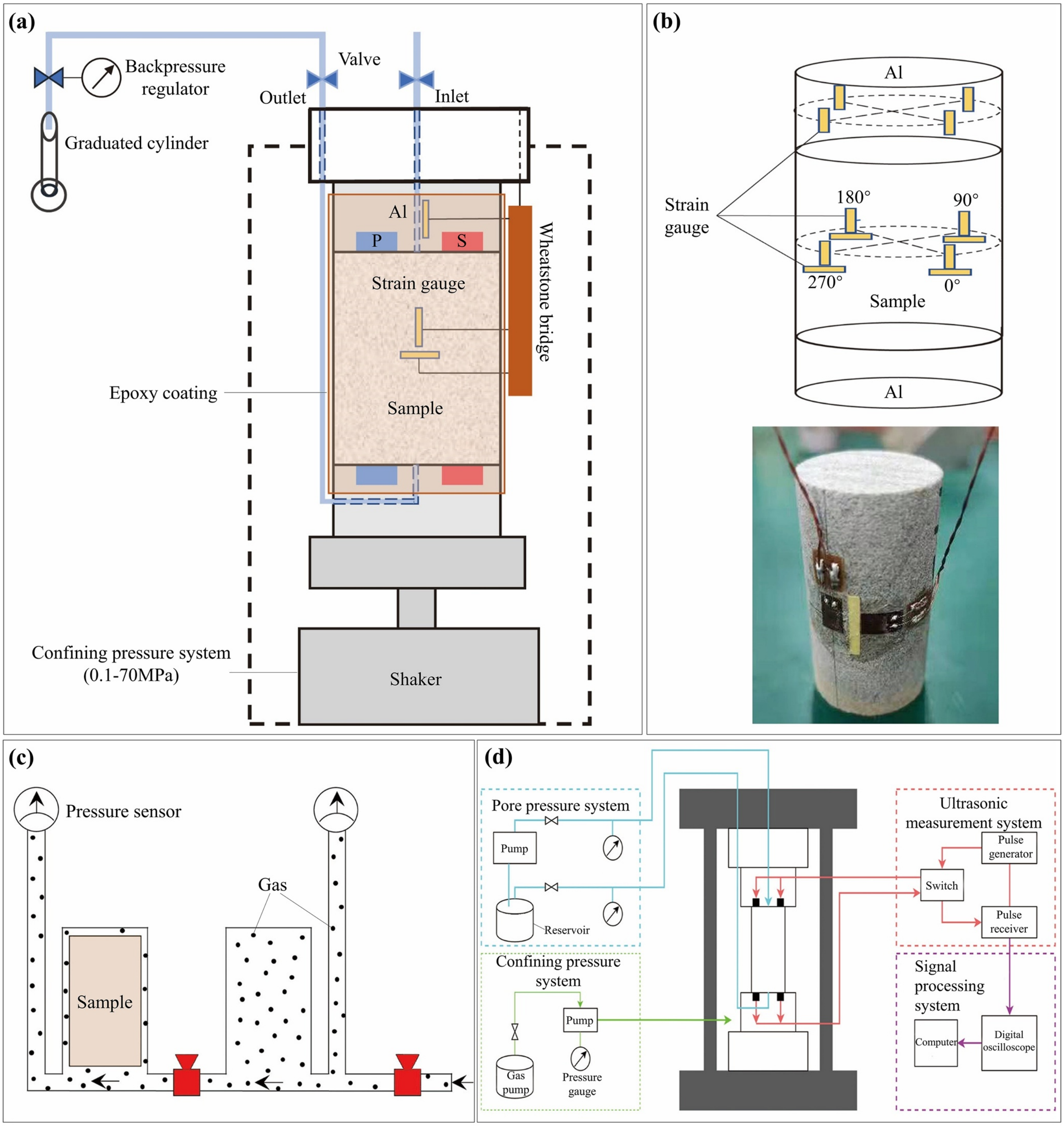

Figure 2. Schematic diagram of (a) the stress-strain measurement system, (b) strain gauges arrangement, adapted from Zhao et al. (2019), (c) the helium porosimeter permeameter adapted from Raymond et al. (2017), and (d) the ultrasonic test setup.

shows an opposite behavior, which may be related to the presence of pore fluid (e.g., Akamatsu et al., 2023; Guéguen & Kachanov, 2011).

3.3. Frequency-Dependent Elastic Wave Velocities

The velocities V_P and V_S are computed with the measured E, ν, and density, assuming isotropy. The results computed with the forced oscillations at 1–100 Hz and the ultrasonic method at 10^6 Hz are given in Figure 5. The

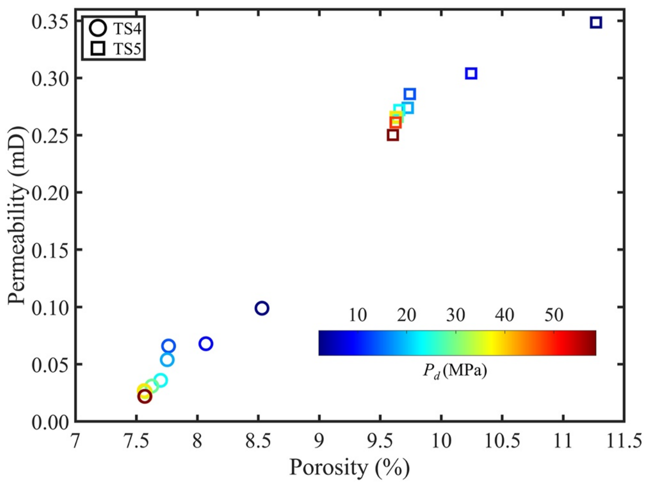

Figure 3. Permeability versus porosity for samples TS4 and TS5. The color bar represents the differential pressure.

values ($V_{\mathrm{P,Dry}}$ and $V_{\mathrm{S,Dry}}$) are nearly constant at dry conditions, while a noticeable wave dispersion (see $V_{\mathrm{P,Sat}}$ and $V_{\mathrm{S,Sat}}$) is observed with water saturation at 1–100 Hz. The P-wave dispersions (~13.3% and 9.7%) are stronger than the S-wave ones (~12% and 5.1%).

4. Theory

4.1. Wave Propagation Theory for Porous Media With Multiscale Cracks

Several experimental and theoretical studies have shown that rocks in the subsurface have different sizes and shapes of pores and fractures (e.g., Cheng & Toksöz, 1979; Hadley, 1976; Sprunt & Brace, 1974; Wang & Tang, 2021). In this study, the pore geometry is considered as a combination of a set of cracks of different aspect ratio α_m (m = 1,2,⋯,M) with volume fraction c_m as well as pores of aspect ratio α_k (k = 1,2,⋯,K) with volume fraction c_k. The aspect ratio of the cracks is less than 0.01, while those of the pores are between 0.01 and 1. Since the differences in the physical properties of regions with different pores are small, the effect of local fluid flow between pores on wave anelasticity is neglected here.

Similar to the differential effective medium (DEM) approach (Norris, 1985), a model for porous media with multiscale cracks is proposed, that is, cracks (inclusions) with the same aspect ratio and radius are gradually embedded in a host medium with pores. For the mth addition, the volume fractions of the host and inclusion phases in such a new cracked porous medium are then $v_{\mathrm{H},m} = (v_{\mathrm{H}} + v_1 + \cdots + v_{m-1})/(v_{\mathrm{H}} + v_1 + \cdots + v_m)$ and $v_{\mathrm{c},m} = v_m/(v_{\mathrm{H}} + v_1 + \cdots + v_m)$, where $v_m = c_m/\phi_{\mathrm{c0}}$ is the volume fraction of regions containing cracks, v_{H} and ϕ_{H0} (ϕ_{c0}) are volume fraction and matrix porosity of the initial host medium (inclusion), respectively. The corresponding absolute porosities are $\phi_{\mathrm{H},m} = \phi_{\mathrm{T},m-1}v_{\mathrm{H},m}$ and $\phi_{\mathrm{c},m} = \phi_{\mathrm{c0}}v_{\mathrm{c,m}}$, and the total porosity is $\phi_{\mathrm{T},m} = \phi_{\mathrm{H},m} + \phi_{\mathrm{c},m}$. Considering that the equivalent response of such a medium can be described by the poroelasticity theory proposed by Zhang, Ba, Carcione, et al. (2019), where cracks are represented by penny-shaped inclusions with random orientation. The strain energy of such a medium is

$$2W = \left(\overline{A} + 2\overline{N}\right)I_1^2 - 4\overline{N}I_2 + 2\overline{Q}_{\mathrm{H}}I_1(\xi_{\mathrm{H}} + \phi_{\mathrm{c},m}\zeta) + \overline{R}_{\mathrm{H}}(\xi_{\mathrm{H}} + \phi_{\mathrm{c},m}\zeta)^2 + 2\overline{Q}_{\mathrm{c}}I_1(\xi_{\mathrm{c}} - \phi_{\mathrm{H},m}\zeta) + \overline{R}_{\mathrm{c}}(\xi_{\mathrm{c}} - \phi_{\mathrm{H},m}\zeta)^2 \tag{1}$$

where I_1 and I_2 are the first and second strain invariants of the frame, respectively, and ξ_{H} (ξ_{c}) is the fluid strain in the host medium (inclusions phase). The scalar ζ is the fluid strain increment between the host medium and inclusions, given by $\zeta = 1/\phi_{\mathrm{H},m}\left(1 - r_m^2/r^2\right)$ and r is the dynamic radius of the inclusions. The stiffness coefficients are

$$\overline{A} = (1 - \phi_{\mathrm{H},m} - \phi_{\mathrm{c},m})K_{\mathrm{g}} - \frac{2}{3}\overline{N} - \overline{Q}_{\mathrm{H}}K_{\mathrm{g}}/K_f - \overline{Q}_{\mathrm{c}}K_{\mathrm{g}}/K_f \tag{2a}$$

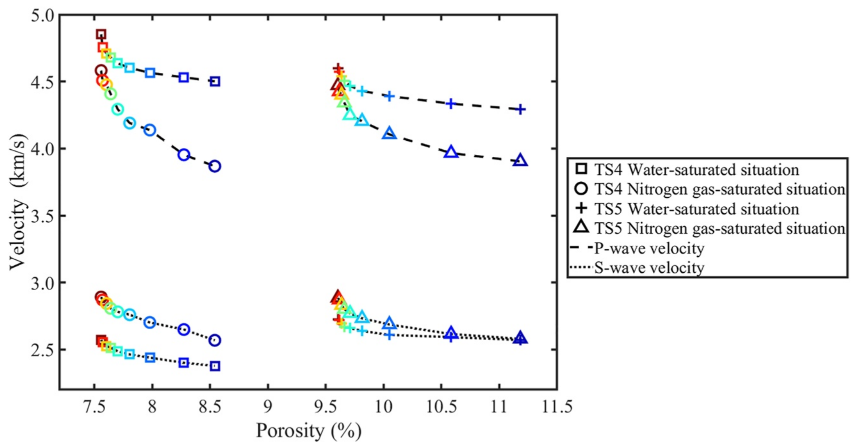

Figure 4. P-wave and S-wave velocities versus porosity for samples TS4 and TS5 at nitrogen gas-saturated and water-saturated conditions.

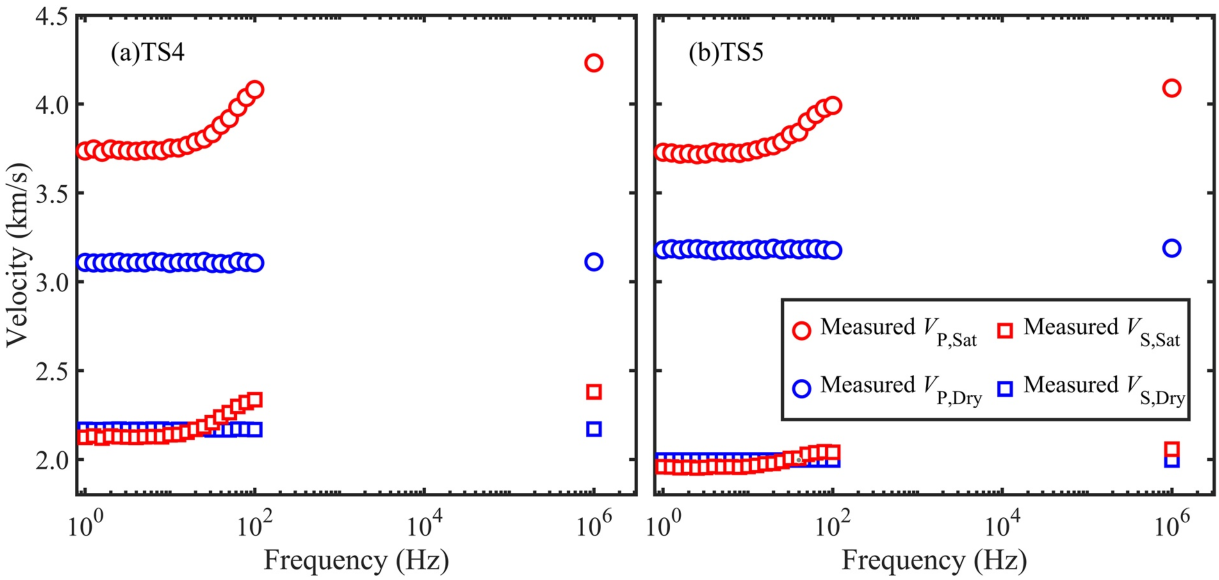

Figure 5. P-wave and S-wave velocities versus frequency for samples TS4 (a) and TS5 (b) at dry and water-saturation situations.

$$\overline{N} = G_b \tag{2b}$$

$$\overline{Q}_{\mathrm{H}} = \frac{\beta\left(1 - \phi_{\mathrm{H},m} - \phi_{\mathrm{c},m} - K_b/K_{\mathrm{g}}\right)\phi_{\mathrm{H},m}K_{\mathrm{g}}}{\beta\left(1 - \phi_{\mathrm{H},m} - \phi_{\mathrm{c},m} - K_b/K_{\mathrm{g}}\right) + K_{\mathrm{g}}/K_f(\beta\phi_{\mathrm{H},m} + \phi_{\mathrm{c},m})} \tag{2c}$$

$$\overline{Q}_{\mathrm{c}} = \frac{\left(1 - \phi_{\mathrm{H},m} - \phi_{\mathrm{c},m} - K_b/K_{\mathrm{g}}\right)\phi_{\mathrm{c},m}K_{\mathrm{g}}}{1 - \phi_{\mathrm{H},m} - \phi_{\mathrm{c},m} - K_b/K_{\mathrm{g}} + K_{\mathrm{g}}/K_f(\beta\phi_{\mathrm{H},m} + \phi_{\mathrm{c},m})} \tag{2d}$$

$$\overline{R}_{\mathrm{H}} = \frac{(\beta\phi_{\mathrm{H},m} + \phi_{\mathrm{c},m})\phi_{\mathrm{H},m}K_{\mathrm{g}}}{\beta\left(1 - \phi_{\mathrm{H},m} - \phi_{\mathrm{c},m} - K_b/K_{\mathrm{g}}\right) + K_{\mathrm{g}}/K_f(\beta\phi_{\mathrm{H},m} + \phi_{\mathrm{c},m})} \tag{2e}$$

$$\overline{R}_{\mathrm{c}} = \frac{(\beta\phi_{\mathrm{H},m} + \phi_{\mathrm{c},m})\phi_{\mathrm{c},m}K_{\mathrm{g}}}{1 - \phi_{\mathrm{H},m} - \phi_{\mathrm{c},m} - K_b/K_{\mathrm{g}} + K_{\mathrm{g}}/K_f(\beta\phi_{\mathrm{H},m} + \phi_{\mathrm{c},m})} \tag{2f}$$

$$\beta = \frac{\phi_{\mathrm{c}0}}{\phi_{\mathrm{H}0}}\left[\frac{1 - (1 - \phi_{\mathrm{H}0})K_{\mathrm{g}}/K_{b\mathrm{H}}}{1 - (1 - \phi_{\mathrm{c}0})K_{\mathrm{g}}/K_{b\mathrm{c}}}\right] \tag{2g}$$

where K_{g}, K_f, and $K_{b\mathrm{H}}$ ($K_{b\mathrm{c}}$) are the grain, fluid, and dry-rock bulk moduli of the initial host medium (inclusion), respectively, and K_b (G_b) is the bulk (shear) modulus of the dry rock, estimated by using Biot-consistent theory (Thomsen, 1985).

The corresponding kinetic energy (T) and dissipation (D) functions are

$$2T = \overline{\rho}_{00}\sum_i \dot{u}_i^2 + 2\overline{\rho}_{01}\sum_i \dot{u}_i\dot{U}_{\mathrm{H},i} + 2\overline{\rho}_{02}\sum_i \dot{u}_i\dot{U}_{\mathrm{c},i} + \overline{\rho}_{11}\sum_i \dot{U}_{\mathrm{H},i}^2 + \overline{\rho}_{22}\sum_i \dot{U}_{\mathrm{c},i}^2 + 2T_{\mathrm{LFF}} \tag{3}$$

$$2D = \frac{\phi_{\mathrm{H},m}\phi_{\mathrm{H}0}\eta}{\kappa_{\mathrm{H}}}\left(\dot{\mathbf{u}} - \dot{\mathbf{U}}_{\mathrm{H}}\right)\left(\dot{\mathbf{u}} - \dot{\mathbf{U}}_{\mathrm{H}}\right) + \frac{\phi_{\mathrm{c},m}\phi_{\mathrm{c}0}\eta}{\kappa_{\mathrm{c}}}\left(\dot{\mathbf{u}} - \dot{\mathbf{U}}_{\mathrm{c}}\right)\left(\dot{\mathbf{u}} - \dot{\mathbf{U}}_{\mathrm{c}}\right) + 2D_{\mathrm{LFF}} \tag{4}$$

where the kinetic energy (T_{LFF}) and dissipation (D_{LFF}) functions related to the WIFF are

$$T_{\mathrm{LFF}} = \frac{3}{16}\rho_f\phi_{\mathrm{H},m}^2\phi_{\mathrm{c},m}r_m^2\dot{\zeta}^2 + \frac{1}{4}\rho_f\frac{\phi_{\mathrm{H},m}^2\phi_{\mathrm{c},m}\phi_{\mathrm{c}0}}{\phi_{\mathrm{H}0}}\ln\frac{l_m + r_m}{r_m}r_m^2\dot{\zeta}^2 \tag{5}$$

$$D_{\mathrm{LFF}} = \frac{3}{16}\frac{\eta\phi_{\mathrm{H},m}^2\phi_{\mathrm{c}0}\phi_{\mathrm{c},m}}{\kappa_{\mathrm{c}}}r_m^2\dot{\zeta}^2 + \frac{1}{4}\frac{\eta\phi_{\mathrm{H},m}^2\phi_{\mathrm{I}0}\phi_{\mathrm{c},m}}{\kappa_{\mathrm{H}}}\ln\frac{l_m + r_m}{r_m}r_m^2\dot{\zeta}^2 \tag{6}$$

where $\mathbf{u}$, $\mathbf{U}_{\mathrm{H}}$, and $\mathbf{U}_{\mathrm{c}}$ are the solid and fluid displacements in the host medium and inclusion phase, respectively. An overdot denotes a time derivative. Moreover, $l_m = \left(r_m^2/12\right)^{1/2}$ is the characteristic fluid-flow length (Pride et al., 2004). The density coefficients are

$$\overline{\rho}_{00} = (1 - \phi_{\mathrm{H},m} - \phi_{\mathrm{c},m})\rho_{\mathrm{g}} - \overline{\rho}_{01} - \overline{\rho}_{02} \tag{7a}$$

$$\overline{\rho}_{01} = \phi_{\mathrm{H},m}\rho_f - \overline{\rho}_{11} \tag{7b}$$

$$\overline{\rho}_{02} = \phi_{\mathrm{c},m}\rho_f - \overline{\rho}_{22} \tag{7c}$$

$$\overline{\rho}_{11} = \frac{1}{2}\left(1 + \frac{1}{\phi_{\mathrm{H0}}}\right)\phi_{\mathrm{H},m}\rho_f \tag{7d}$$

$$\overline{\rho}_{22} = \frac{1}{2}\left(1 + \frac{1}{\phi_{\mathrm{c0}}}\right)\phi_{\mathrm{c},m}\rho_f \tag{7e}$$

where ρ_{g} and ρ_f are the grain and fluid densities, respectively. η is the fluid viscosity. κ_{H} and κ_{c} are the permeabilities of the host medium and inclusion phase, respectively.

By considering that $\phi_{\mathrm{c},m}$ is much smaller than $\phi_{\mathrm{H},m}$, the high-order terms of $\phi_{\mathrm{c},m}$ can be neglected. The dynamic equations derived from Hamilton's principle can then be expressed as follows.

$$\begin{aligned}
&(N + NS\phi_{\mathrm{c},m})\nabla^2\mathbf{u} + (A+N)\nabla e + (A_{\mathrm{d}} + NS)\phi_{\mathrm{c},m}\nabla e + Q_{\mathrm{H}}\phi_{\mathrm{H},m}\nabla(\xi_{\mathrm{H}} + \phi_{\mathrm{c},m}\zeta) \\
&+ R_{\mathrm{H}}\left(\frac{Q_{\mathrm{c}}}{K_f} - \frac{Q_{\mathrm{c}}}{K_{\mathrm{g}}} - 1\right)\phi_{\mathrm{c},m}\nabla\xi_{\mathrm{H}} + Q_{\mathrm{c}}\phi_{\mathrm{c},m}\nabla(\xi_{\mathrm{c}} - \phi_{\mathrm{H},m}\zeta) \\
&= \rho_{00}\ddot{\mathbf{u}} + \left(\rho_{00}S - \rho_{\mathrm{g}} - \rho_{02}\right)\phi_{\mathrm{c},m}\ddot{\mathbf{u}} + \rho_{01}\phi_{\mathrm{H},m}\ddot{\mathbf{U}}_{\mathrm{H}} + \rho_{01}\phi_{\mathrm{H},m}S\phi_{\mathrm{c},m}\ddot{\mathbf{U}}_{\mathrm{H}} + \rho_{02}\phi_{\mathrm{c},m}\ddot{\mathbf{U}}_{\mathrm{c}} \\
&+ \frac{\phi_{\mathrm{H},m}\phi_{\mathrm{H0}}\eta}{\kappa_{\mathrm{H}}}\left(\dot{\mathbf{u}} - \dot{\mathbf{U}}_{\mathrm{H}}\right) + \frac{\phi_{\mathrm{H},m}\phi_{\mathrm{H0}}\eta}{\kappa_{\mathrm{H}}}S\phi_{\mathrm{c},m}\left(\dot{\mathbf{u}} - \dot{\mathbf{U}}_{\mathrm{H}}\right) + \frac{\phi_{\mathrm{c0}}\eta\phi_{\mathrm{c},m}}{\kappa_{\mathrm{c}}}\left(\dot{\mathbf{u}} - \dot{\mathbf{U}}_{\mathrm{c}}\right)
\end{aligned} \tag{8a}$$

$$\begin{aligned}
&Q_{\mathrm{H}}\nabla e + R_{\mathrm{H}}\nabla(\xi_{\mathrm{H}} + \phi_{\mathrm{c},m}\zeta) + \frac{R_{\mathrm{H}}}{\phi_{\mathrm{H},m}}\left(\frac{1}{\beta}\nabla\xi_{\mathrm{H}} - \nabla e\right)\phi_{\mathrm{c},m} \\
&= \left(1 + \frac{R_{\mathrm{H}}}{\phi_{\mathrm{H},m}}\left(\frac{1}{\beta K_f} - \frac{1}{K_{\mathrm{g}}}\right)\phi_{\mathrm{c},m}\right)\left(\rho_{01}\ddot{\mathbf{u}} + \rho_{11}\ddot{\mathbf{U}}_{\mathrm{H}} - \frac{\phi_{\mathrm{H0}}\eta}{\kappa_{\mathrm{H}}}\left(\dot{\mathbf{u}} - \dot{\mathbf{U}}_{\mathrm{H}}\right)\right)
\end{aligned} \tag{8b}$$

$$Q_{\mathrm{c}}\nabla e + R_{\mathrm{c}}\nabla(\xi_{\mathrm{c}} - \phi_{\mathrm{H},m}\zeta) = \rho_{02}\ddot{\mathbf{u}} + \rho_{22}\ddot{\mathbf{U}}_{\mathrm{c}} - \frac{\phi_{\mathrm{c0}}\eta}{\kappa_{\mathrm{c}}}\left(\dot{\mathbf{u}} - \dot{\mathbf{U}}_{\mathrm{c}}\right) \tag{8c}$$

$$\begin{aligned}
&(Q_{\mathrm{H}}e + R_{\mathrm{H}}(\xi_{\mathrm{H}} + \zeta\phi_{\mathrm{c},m})) - (Q_{\mathrm{c}}e + R_{\mathrm{c}}(\xi_{\mathrm{c}} - \phi_{\mathrm{H},m}\zeta)) \\
&= \left(\frac{3}{8} + \frac{\phi_{\mathrm{c0}}}{2\phi_{\mathrm{H0}}}\ln\frac{r_m + l_m}{r_m}\right)\phi_{\mathrm{H},m}\rho_f r_m^2\ddot{\zeta} + \left(\frac{3\eta}{8\kappa_{\mathrm{c}}} + \frac{\eta}{2\kappa_{\mathrm{H}}}\ln\frac{r_m + l_m}{r_m}\right)\phi_{\mathrm{c0}}\phi_{\mathrm{H},m}r_m^2\dot{\zeta}
\end{aligned} \tag{8d}$$

where e is the solid divergence field.

The stiffnesses are

$$A = (1 - \phi_{\mathrm{H},m})K_{\mathrm{g}} - \frac{2}{3}N - K_{\mathrm{g}}/K_f Q_{\mathrm{H}}\phi_{\mathrm{H},m} \tag{9a}$$

$$A_{\mathrm{d}} = (1 - \phi_{\mathrm{H},m})K_{\mathrm{g}}S - \frac{2}{3}NS - Q_{\mathrm{c}}R_{\mathrm{H}}\left(K_{\mathrm{g}}/K_f^2 - 1/K_f\right) - (Q_{\mathrm{c}} - R_{\mathrm{H}})K_{\mathrm{g}}/K_f - K_{\mathrm{g}} \tag{9b}$$

$$N = G_{\mathrm{b}} \tag{9c}$$

$$Q_{\mathrm{H}} = \frac{K_{\mathrm{g}}\left(1 - \phi_{\mathrm{H},m} - K_b/K_{\mathrm{g}}\right)}{1 - \phi_{\mathrm{H},m} - K_b/K_{\mathrm{g}} + K_{\mathrm{g}}/K_f\phi_{\mathrm{H},m}} \tag{9d}$$

$$Q_{\mathrm{c}} = \frac{K_{\mathrm{g}}\left(1 - \phi_{\mathrm{H},m} - K_b/K_{\mathrm{g}}\right)}{1 - \phi_{\mathrm{H},m} - K_b/K_{\mathrm{g}} + K_{\mathrm{g}}/K_f\beta\phi_{\mathrm{H},m}} \tag{9e}$$

$$R_{\mathrm{H}} = \frac{K_{\mathrm{g}}\phi_{\mathrm{H},m}}{1-\phi_{\mathrm{H},m}-K_b/K_{\mathrm{g}}+K_{\mathrm{g}}/K_f\phi_{\mathrm{H},m}} \tag{9f}$$

$$R_{\mathrm{c}} = \frac{K_{\mathrm{g}}\beta\phi_{\mathrm{H},m}}{1-\phi_{\mathrm{H},m}-K_b/K_{\mathrm{g}}+K_{\mathrm{g}}/K_f\beta\phi_{\mathrm{H},m}} \tag{9g}$$

$$S = R_{\mathrm{H}}/\phi_{\mathrm{H},m}\left(1/\beta/K_f - 1/K_{\mathrm{g}}\right) + R_{\mathrm{c}}/\beta/\phi_{\mathrm{H},m}\left(1/K_f - 1/K_{\mathrm{g}}\right) \tag{9h}$$

and the density coefficients are

$$\rho_{00} = (1-\phi_{\mathrm{H},m})\rho_{\mathrm{g}} - \rho_{01} \tag{10a}$$

$$\rho_{01} = \frac{1}{2}\left(1-\frac{1}{\phi_{\mathrm{H}0}}\right)\rho_f \tag{10b}$$

$$\rho_{02} = \frac{1}{2}\left(1-\frac{1}{\phi_{\mathrm{c}0}}\right)\rho_f \tag{10c}$$

$$\rho_{11} = \frac{1}{2}\left(1+\frac{1}{\phi_{\mathrm{H}0}}\right)\rho_f \tag{10d}$$

$$\rho_{22} = \frac{1}{2}\left(1+\frac{1}{\phi_{\mathrm{c}0}}\right)\rho_f \tag{10e}$$

The dispersion equations can be obtained by substituting plane P-wave or S-wave kernels into Equation 8 (see Equations B1–B4 in Ba et al. (2011)). Then, the P-wave and S-wave complex wavenumbers (k_P and k_S) are computed from the dispersion equations. Finally, the complex bulk and shear moduli of the cracked porous medium are

$$K_{\mathrm{sat}} = \left((1-\phi_{\mathrm{H,m}}-\phi_{c,\mathrm{m}})\rho_{\mathrm{g}} + (\phi_{\mathrm{H,m}}+\phi_{c,\mathrm{m}})\rho_f\right)\left(\frac{\omega}{k_P}\right)^2 - \frac{4}{3}G_{\mathrm{sat}} \tag{11a}$$

$$G_{\mathrm{sat}} = \left((1-\phi_{\mathrm{H,m}}-\phi_{c,\mathrm{m}})\rho_{\mathrm{g}} + (\phi_{\mathrm{H,m}}+\phi_{c,\mathrm{m}})\rho_f\right)\left(\frac{\omega}{k_S}\right)^2 \tag{11b}$$

where ω is the angular frequency.

The dry-rock complex moduli at the end of each addition, which are considered as the moduli of the new host medium in the next step, are estimated from the complex wet-rock moduli by using the inverse Gassmann equations (Gassmann, 1951).

$$\frac{K_{\mathrm{sat}}}{K_{\mathrm{g}}-K_{\mathrm{sat}}} = \frac{K_{\mathrm{b}}}{K_{\mathrm{g}}-K_{\mathrm{b}}} + \frac{K_f}{(\phi_{\mathrm{H,m}}+\phi_{c,\mathrm{m}})\left(K_{\mathrm{g}}-K_f\right)} \tag{12a}$$

$$G_{\mathrm{b}} = G_{\mathrm{sat}} \tag{12b}$$

By using Equations 8–12 at each addition and stopping the addition procedure when all the cracks are added, the P-wave and S-wave velocity and quality factor of the water-saturated rock as a function of frequency can be obtained, as

$$V_{\mathrm{P,S}} = \left[\mathrm{Re}\left(\frac{k_{\mathrm{P,S}}}{\omega}\right)\right]^{-1} \text{ and } Q_{\mathrm{P,S}} = \frac{\mathrm{Re}(\omega/k_{\mathrm{P,S}})}{2\mathrm{Im}(\omega/k_{\mathrm{P,S}})} \tag{13}$$

respectively.

4.2. Estimation of Pore Geometry

Considering that the volume fraction of the pores/cracks varies with the pressure, the following is obtained (Toksöz et al., 1976)

$$\frac{dc(\alpha)}{c(\alpha)} = -\frac{P_d/K_A^*}{E_1 - \frac{E_2E_3}{E_3+E_4}} \tag{14}$$

where K_A^* is the dry-rock effective static bulk modulus, E_1–E_4 are functions of α and the effective matrix moduli. These quantities are usually substituted with the dry-rock effective dynamic moduli (e.g., Cheng & Toksöz, 1979; Yan et al., 2014). Hence, the volume fraction and aspect ratio of a set of pores/cracks at varying pressure $P_{d,n}$ ($n = 1,2,\ldots,N$) are related to $c_{0l} = [c_k;c_m]$ and $\alpha_{0l} = [\alpha_k;\alpha_m]$ at zero differential pressure as (Cheng, 1978)

$$c_{nl} = c_{0l}\left(1 + \frac{\mathrm{d}c}{c}(\alpha_{0l}, P_{d,n})\right) \tag{15}$$

and

$$\alpha_{nl} = \alpha_{0l}\left(1 + \frac{\mathrm{d}c}{c}(\alpha_{0l}, P_{d,n})\right) \tag{16}$$

respectively. When $d\alpha/\alpha \le -1$, the pores/cracks are considered to be closed. Therefore, the frequency-dependent wave velocity and attenuation at different pressures can be determined using Equations 8, 15, and 16. Conversely, a pore geometry can be determined from these measurements. To ensure that the inverted pore geometry is more realistic, the experimental pressure-dependent velocities in the nitrogen gas case are a constraint (these measurements can be modeled using the multiphase DEM model proposed by Han (2016)). Then, a cost function F is given, which must be minimized between the experimental and modeled values as

$$\begin{aligned} &F_{ela}\left(\alpha_{01}, \alpha_{02}, \cdots\alpha_{0n}, c_{01}, c_{02}, \cdots c_{0n}, r_{01}, r_{02}, \cdots r_{0m}, K_g, \mu_g\right) \\ &= \min\left[\sum_{n=1}^{N}\left(V_{Pn}^{\mathrm{Mea}} - V_{Pn}^{\mathrm{Pre}}\right)_{\mathrm{Ng}}^2 + \sum_{n=1}^{N}\left(V_{Sn}^{\mathrm{Mea}} - V_{Sn}^{\mathrm{Pre}}\right)_{\mathrm{Ng}}^2 + \sum_{n=1}^{N}\sum_{t=1}^{T}\left(V_{Pn,t}^{\mathrm{Mea}} - V_{Pn,t}^{\mathrm{Pre}}\right)_{\mathrm{sat}}^2\right] \end{aligned} \tag{17}$$

where T is the number of measurement frequencies, V_{Pn}^{Mea} and V_{Sn}^{Mea} are the measured P-wave and S-wave velocities at the nth differential pressure, respectively, and V_{Pn}^{Pre} and V_{Sn}^{Pre} are the corresponding theoretical (predicted) values. The subscripts "Ng" and "sat" represent the nitrogen gas and water-saturation cases, respectively. Since it was considered unreasonable to use a mineral bulk modulus or an average modulus estimated from the Voigt-Reuss-Hill average as the grain elasticity modulus (Qin et al., 2022), they are also unknown in the modeling process. Equation 17 is minimized using the simulated annealing method (e.g., Ingber, 1993).

5. Examples

5.1. TS4 and TS5 Samples

The modeling results have been compared to the velocity measurements of samples TS4 and TS5 in Figures 6 and 7, respectively. The inverted grain bulk (shear) moduli are 32.6 (29.8) and 32.06 (31.4) GPa for TS4 and TS5, respectively. The basic properties of the two samples are shown in Table 1.

Figures 6a and 7a show that the theoretical velocities of the nitrogen-gas cases agree with the measurements (at the measurement frequency of 0.5 MHz), with $R^2 = 0.933$ ($V_{\mathrm{P,Ng}}$) and 0.829 ($V_{\mathrm{S,Ng}}$) for sample TS4, and 0.983 and 0.971 for sample TS5. The estimated pore-aspect-ratio spectrum is used as an input of the multiphase DEM model to compute the velocities of the water-saturation case at different differential pressures. The modeling results agree with the measured $V_{\mathrm{P,Sat}}$ with $R^2 = 0.777$ and 0.933 for samples TS4 and TS5, respectively. At the wave frequency of 0.5 MHz, there is unrelaxation of local fluid flow, except that between pores and cracks with a maximum $\alpha_{max} = 0.0032$ (see Figures 6c and 7c; in this case, the characteristic frequency is 1 MHz according to O'Connell and Budiansky (1977)). The theoretical $V_{\mathrm{S,Sat}}$ is higher than the measurement, which may be related to the presence of a shear-weakening effect, that is, a chemical reaction between the fluid and clay minerals during the saturation experiment (Clark et al., 1980; Pimienta et al., 2014; Yin et al., 2019). Another cause may be that multiphase DEM mode provides an upper bound for the elastic moduli (David & Zimmerman, 2012).

Figures 6b and 7b show that the model provides a good match of the measured $V_{\mathrm{P,sat}}$ as a function of frequency (where the differential pressure is 0 MPa), while it cannot describe the dispersion behavior of the S-wave. This is because when the S-wave propagates through water-saturated rocks, cracks with certain orientations can be compressed and there is then a dispersion of the S-wave caused by the flow of pore fluid between pores/cracks

AGU ADVANCING EARTH AND SPACE SCIENCES
Journal of Geophysical Research: Solid Earth
10.1029/2023JB027474

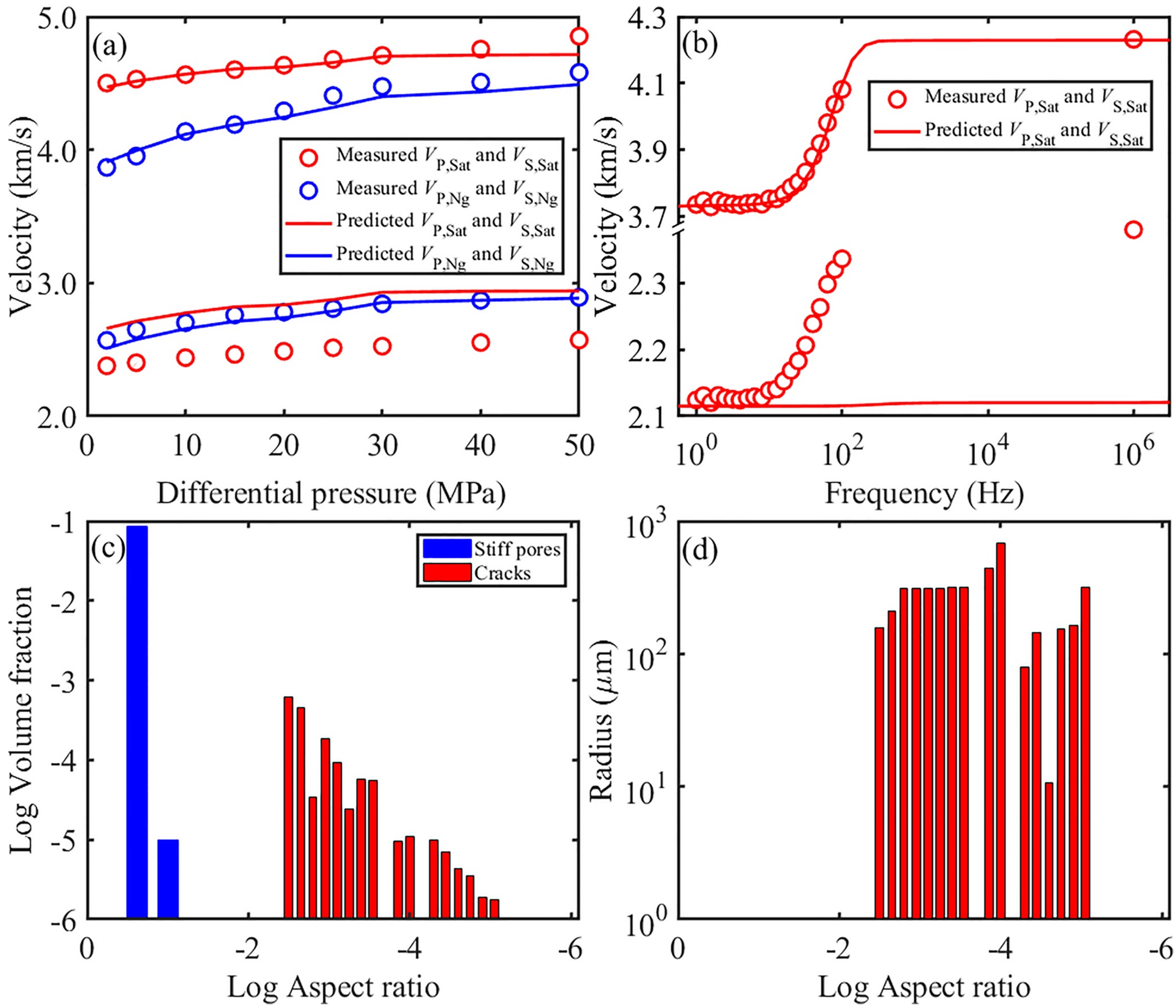

Figure 6. Sample TS4. Comparison between the measured and theoretical velocities versus differential pressure (a) and frequency (b). (c) Estimated pore-aspect-ratio spectrum. (d) Estimated crack-radius spectrum.

and cracks (Quintal et al., 2012). This causes the measured S-wave velocities to be higher than the predicted values, although the presented model does not account for this mechanism. It is also found that the characteristic frequency for the local fluid flow should be about 100 Hz, indicating that the local fluid flow between pores and cracks with an aspect ratio of about 0.000145 is the main factor for the P-wave dispersion.

The pore-aspect-ratio spectra at zero differential pressure are given in Figures 6c and 7c, where the stiff pores with an aspect ratio of 0.24/0.22 are the main contributors. The range of crack aspect ratios are 0.000009–0.0032 and 0.000006–0.0032 for samples TS4 and TS5, respectively. Cracks with smaller aspect ratios close first at low pressures, resulting in the drastic variation of the properties of sample TS5 at the low-pressure range. Furthermore, the estimated crack porosities of the two samples are 0.16% and 0.12%, which are smaller than the values of 1.2% and 2.14% estimated with the measured porosity (see Figure 3). Figures 6 and 7d are the estimated crack radius spectra at zero differential pressure, with radii ranging in the intervals of 10.5–682.8 and 47.2–480 μm. The crack radii may vary by 1~2 orders of magnitude. To verify the results, a comparison with NMR data spectroscopy is shown in Figure 8, where we can see that the estimated crack radii are larger than the NMR values. The reason for such behavior could be related to the fact that the assumption of penny-shaped inclusions cannot

10.1029/2023JB027474

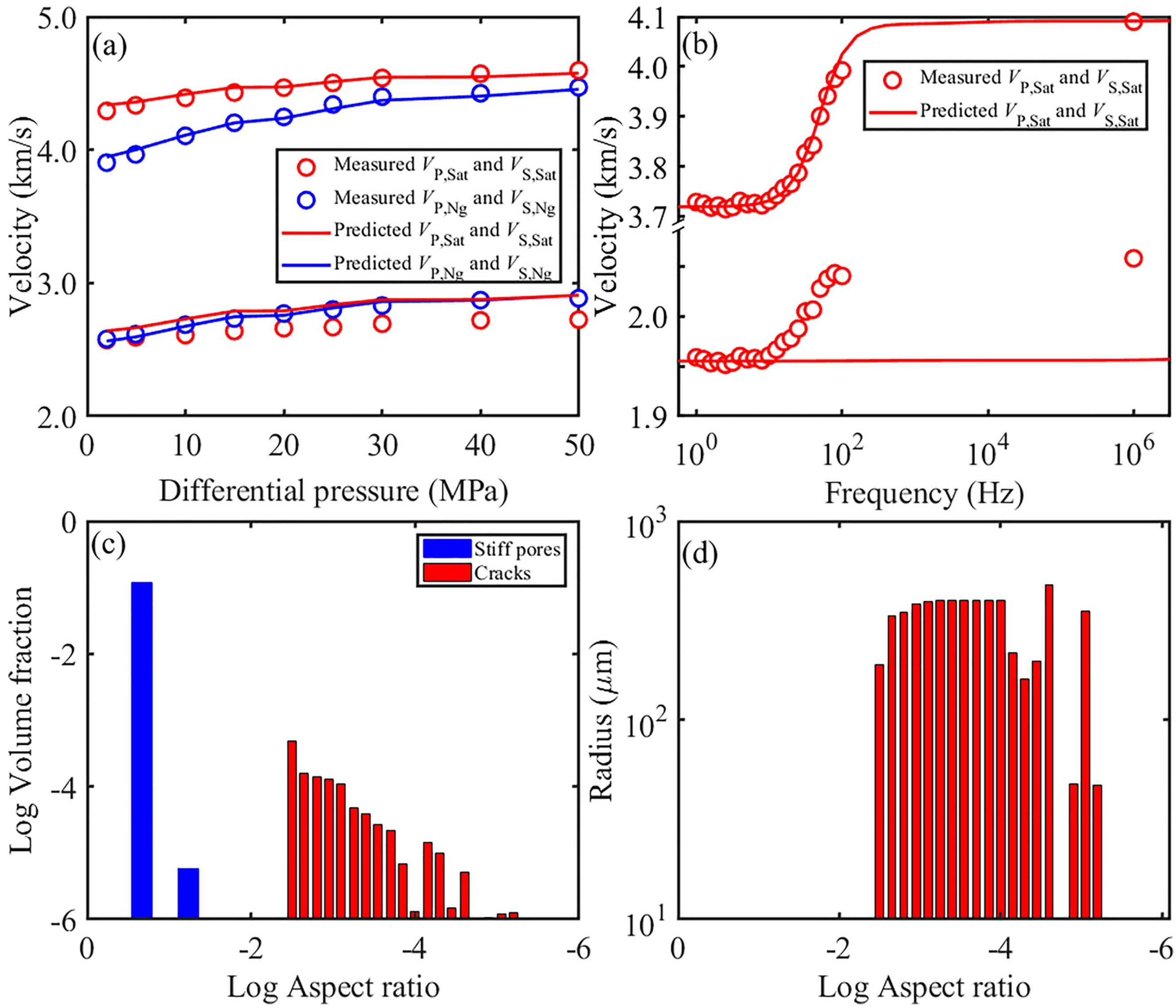

Figure 7. Sample TS5. Comparison between the measured and theoretical velocities versus differential pressure (a) and frequency (b). (c) Estimated pore-aspect-ratio spectrum. (d) Estimated crack-radius spectrum.

fully describe the pore geometries of real rocks. Another possible cause is that the contribution of cracks with a smaller radius to the seismic waves is neglected.

5.2. Comparison Between Modeling Results and Published Data

To further illustrate the performance of the proposed model, comparisons are made with published data from a tight sandstone (Yin et al., 2017) and a low-porosity sandstone (Li et al., 2022). Their porosity, permeability, and grain density are 8.932% and 10.26%, 6.3×10^{-17} and 0.97×10^{-15} m^2, and 2.444 and 2.607 g/cm^3, respectively. The former was measured at various differential pressures up to 35 MPa and a wide frequency band of (2–200, 10^6) Hz for brine-saturated case. The latter was measured at differential pressures of 5–20 MPa and a full-frequency range from 1 to 3,000 Hz for the white oil-saturated case.

Table 1
Properties of TS4 and TS5

Samples	K_{bH} (GPa)	G_{bH} (GPa)	ϕ_{H0} (%)	ϕ_{c0} (%)	κ_H (mD)
TS4	7.6	11.5	8.26	32[a]	0.149
TS5	19.2	9.5	11.3	32[a]	0.3985

[a]From Pride et al. (2004).

10.1029/2023JB027474

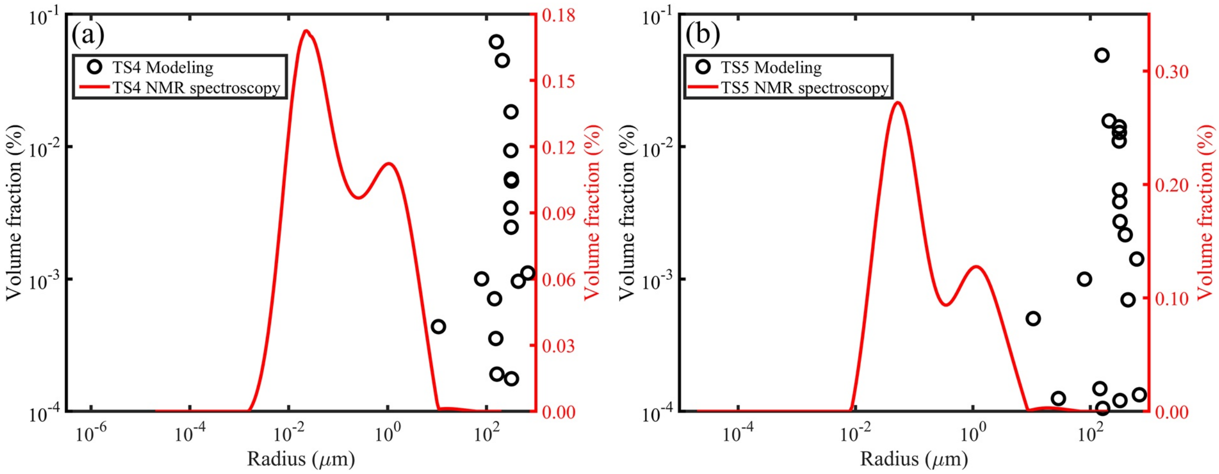

Figure 8. Comparison between the measured and nuclear magnetic resonance (NMR) crack radii for samples TS4 (a) and TS5 (b).

For the tight sandstone, quantities ϕ_{H0} and κ_H are set as 8.9% and 6.3 $\times 10^{-17}$ m^2, respectively. The density, bulk modulus, and viscosity of brine are 1.013 g/cm^3, 2.28 GPa, and 0.001023 Pa·s, respectively. Then, K_{bH} (G_{bH}) are 18.2 (12.3), 20.2 (13.18), 20.8 (13.5), 21.8 (13.88), 22.6 (14.3), 23.3 (14.61), 23.7 (14.83), 24.2 (14.98), and 24.6 (15.15) GPa for P_d = 2, 5, 7, 10, 15, 20, 25, 30, and 35 MPa, respectively. The estimated grain bulk/shear moduli are 30.4 and 20 GPa, respectively.

Figures 9a and 9b show that the predictions are in good agreement with the velocity measurements, unless for $V_{P,Sat}$ at 2 MPa (see Figure 9b). The estimated pore-aspect-ratio spectrum at zero differential pressure is given in Figure 9d, where it shows that pores with aspect ratio of 0.229 dominate, and the crack aspect ratio ranges from 0.0001 to 0.01. The pore-aspect-ratio spectra versus differential pressures can be obtained with Equations 15 and 16. The estimated crack porosity at each pressure is then 3.1×10^{-4}, 2.37×10^{-4}, 1.98×10^{-4}, 1.57×10^{-4}, 1.08×10^{-4}, 7.09×10^{-5}, 4.80×10^{-5}, 3.49×10^{-5}, and 2.77×10^{-5}. It is noted that this sample (8.932%) and TS4 (8.77%) have similar porosity, while the difference in velocity is due to the difference in pore geometry (see Figures 6c and 9d for comparison). Figure 9c compares the measured and theoretical P-wave attenuation, and the predictions describe the measurements well, where the predicted characteristic frequency at the seismic band shifts to lower frequencies from P_d = 2–10 MPa, to higher frequencies from P_d = 10–20 MPa, and to lower frequencies from P_d = 20–35 MPa. The predicted attenuation is smaller than the measurement at low frequencies, which means that there may be additional attenuation mechanisms related to the frame (e.g., Kuteynikova et al., 2014).

Figure 10 shows the crack radius spectra versus differential pressure. With increasing pressure, the radius decreases from P_d = 2 (i.e., 0.05–138 μm) to 7 MPa (i.e., 0.002–1.48 μm), and increases from P_d = 7 to 35 (i.e., 4.6–231 μm) MPa. Similar findings can be seen in Figure 13a of Sarout et al. (2017). To clarify, the crack aperture $2w$ versus differential pressure is computed by using the relation $2w = 2\alpha r$, which is shown in Figure 11. The aperture remains largely unaffected from P_d = 2–10 MPa, while there is an increase from 10 to 35 MPa. This differs from Figure 14a of Sarout et al. (2017), where the aperture decreases for $P_d > 10$ MPa.

For the low-porosity sandstone, ϕ_{H0} and κ_H are 10.2% and 0.97×10^{-15} m^2, respectively. The density, bulk modulus, and viscosity of white oil are 0.83 g/cm^3, 1.4 GPa, and 0.01245 Pa·s, respectively. Then, K_{bH}/G_{bH} are 13/8.1, 19.15/10.25, 22.8/12 and 23.2/13.12 GPa for P_d = 5, 10, 15, and 20 MPa, respectively. The estimated grain bulk/shear moduli are 29.6 and 29.4 GPa, respectively.

Comparison between the measured and theoretical velocities shows that the model describes the measurements well (see Figures 12a and 12b). Figure 12c shows the predicted P-wave attenuation. The two attenuation peaks are observed at P_d = 5 MPa, while only one attenuation peak is seen at other P_d. Similarly, Figure 12d shows the estimated pore-aspect-ratio spectrum, where pores with aspect ratio of 0.12 dominate, and the crack aspect ratio varies between 0.0001 and 0.01. According to Equations 15 and 16, the estimated crack porosity at each pressure is 7.64×10^{-4}, 4.4×10^{-4}, 2.32×10^{-4}, and 1.05×10^{-4}. The crack radius spectra as a function of differential

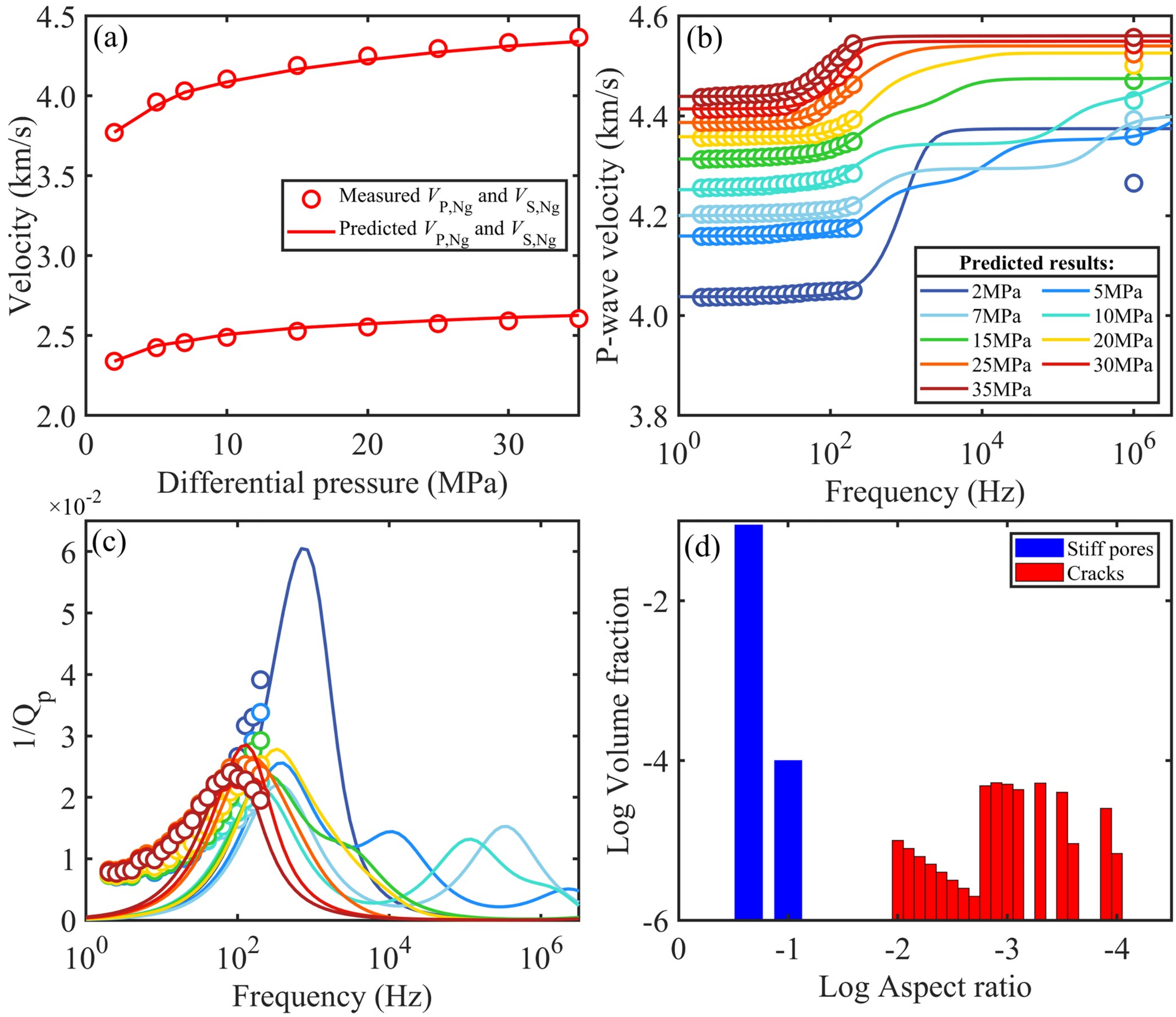

Figure 9. Tight sandstone sample. Comparison between the measured and theoretical wave velocities versus differential pressure (a) and frequency (b). (c) Comparison between the measured and theoretical attenuation versus frequency. (d) Estimated pore-aspect-ratio spectrum.

pressure are given in Figure 13. The distributed radius ranges are 0.048–1,780, 0.034–710.1, 0.04–1,106.23, and 0.055–949.51 μm at each pressure.

6. Discussion

6.1. Assessment of the Modeling Approach

According to Figure 2c of Wang and Tang (2021), the range of crack aspect ratios is 0.0001–0.00148, smaller than that of Figure 9d here. This difference implies that the results depend on the choice of the theoretical approach. To obtain a more realistic spectrum, a comparison with that obtained with SEM and micro X-ray CT could be performed in a future study. In Wang and Tang (2021), the pressure-dependent crack porosity and aspect ratio are the main causes for the measured dispersion trend with respect to pressure, whereas our study shows that the crack radius also affects the characteristic frequency induced by the local fluid flow between pores and cracks. A varying pore structure with pressure (multiscale cracks) can better describe the dispersion and attenuation at a broad frequency range, compared with a model assuming a single set of cracks (see Figure 7b of Yin

10.1029/2023JB027474

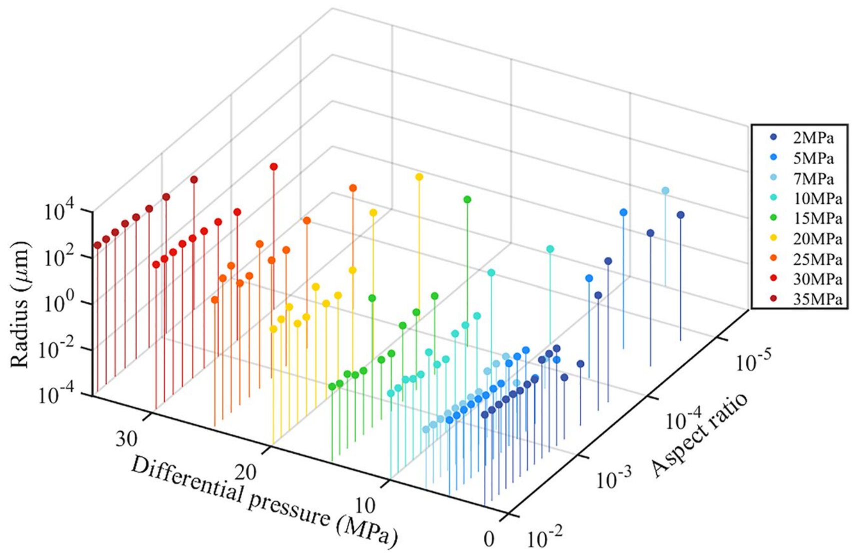

Figure 10. Crack radius spectra versus differential pressure for tight sandstone sample.

et al. (2017)). However, the approach is limited to P-wave dispersion induced by fluid flow between pores and cracks, while flow between cracks is not considered in this work. Guo, Zhao, et al. (2022) derived a theoretical model using the Biot's dynamic poroelasticity equations to analyze the dispersion and attenuation of P-waves caused by FF-WIFF (Fracture-Fracture Wave-induced Fluid Flow). Then, they (Guo, Gurevich, & Chen, 2022) further analyzed the SV-waves using the same approach. Their work can be helpful for us to further extend the multiscale fracture model.

6.2. Assessment of the Estimated Pore Geometry

The properties of pores and cracks can be used to estimate the permeability of the rock. By assuming that pores and cracks are connected in parallel, the rock permeability is divided into two parts: matrix (κ_{p}) and crack (κ_{c}) permeabilities (e.g., Shapiro et al., 2015). If the rock is composed of circular tubes with a pore radius of r_k, then (Al-Wardy & Zimmerman, 2004)

$$\kappa_{\mathrm{p},k} = \frac{c_k r_k^2}{8} \tag{18}$$

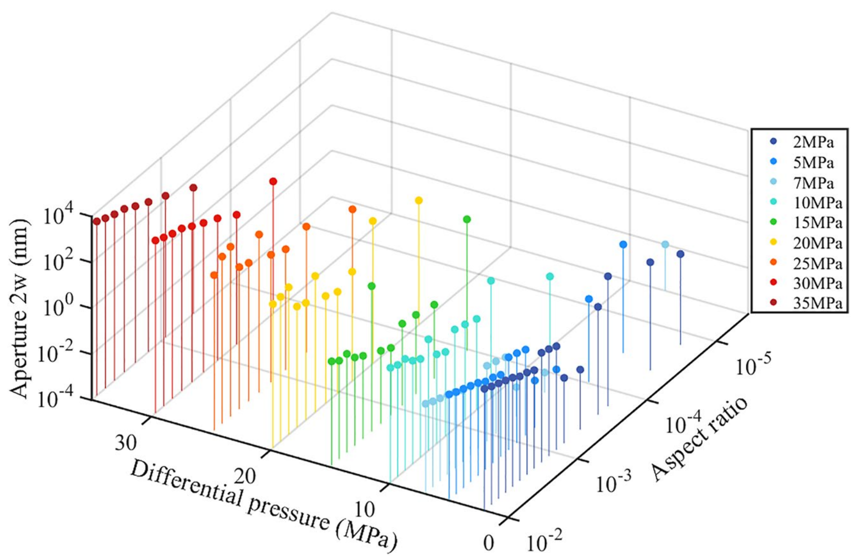

Figure 11. Crack aperture spectra versus differential pressure for tight sandstone sample.

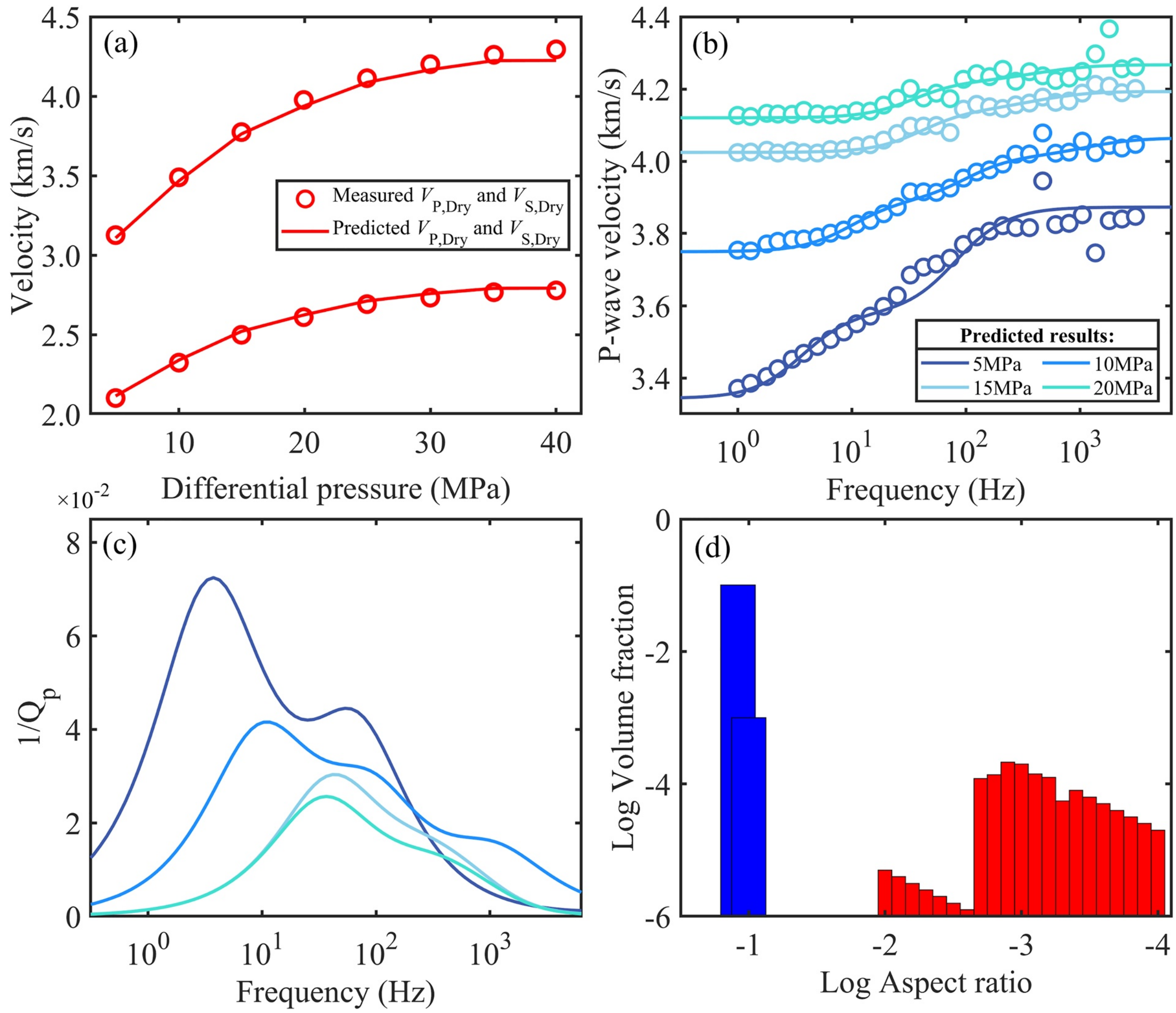

Figure 12. Low-porosity sandstone sample. Comparison between the measured and theoretical velocities versus differential pressure (a) and frequency (b). (c) Theoretical attenuation versus frequency. (d) Estimated pore-aspect-ratio spectrum.

For randomly oriented penny-shaped cracks, we have (Sarout, 2012)

$$\kappa_{c,m} = \frac{16}{27}\frac{c_m r_m^2 \alpha_m^2\left(1-\alpha_m^2\right)}{\left(2\sqrt{1-\alpha_m^2}+\alpha_m^2\log\left(\frac{2-\alpha_m^2+2\sqrt{1-\alpha_m^2}}{\alpha_m^2}\right)\right)^2} \tag{19}$$

For samples TS4 and TS5, the only unknown parameter is the pore radius. It is presumed that all cracks close at the high differential pressure, that radius can be estimated with measurements at $P_d = 50$ MPa by using Equation 18. The estimated radii of the two pore phases are 0.083 (0.15) and 1.2 (0.02) μm for sample TS4 (TS5). The results for the dominant pores are larger than the values of NMR spectroscopy (i.e., 0.023 and 0.05 μm for TS4 and TS5, respectively; see Figure 8). It is noted that the radii vary with pressure and are not constant, according to Figure 10. Hence, the radii at different pressures can be estimated by fitting the measured permeability with Equations 18 and 19. The results by using these equations are shown in Figure 14, compared with the measured data. Results by using pressure-dependent radii are overlain with the measured data, while using radii at zero differential pressure yields smaller values than the measurements at low differential pressures. This difference shows that the assumption that crack radii are constant with differential pressure is not satisfied.

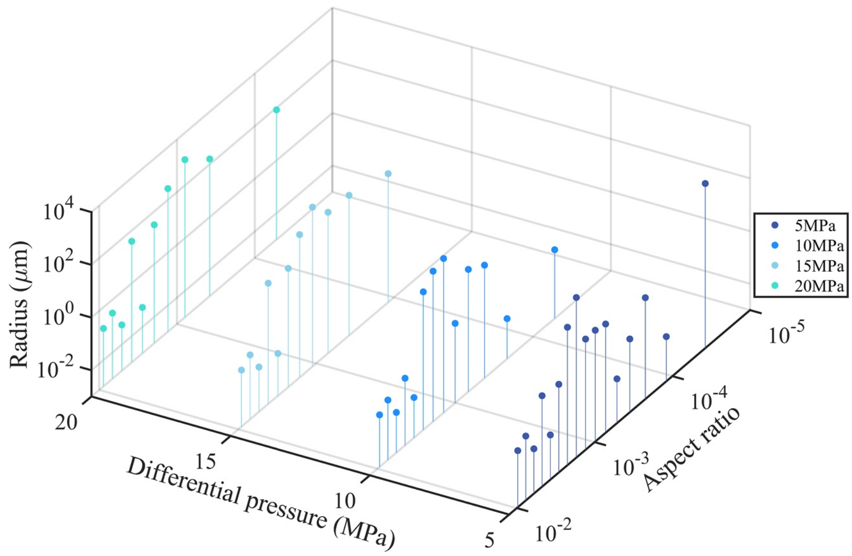

Figure 13. Crack radius spectra versus differential pressure for low-porosity sandstone sample.

7. Conclusions

We have performed the acoustic wave propagation experiments on two tight sandstone samples. The ultrasonic wave velocities vary nonlinearly with differential pressure, and at water-saturation conditions exhibit dispersion at the seismic range (1–100 Hz). To better understand the effects of multiscale cracks on wave anelasticity, we propose a model based on the elastic wave theory with a set of penny-shaped cracks, combined with a multiphase DEM model to estimate the pore geometry, including aspect ratios, radii, and volume fractions of pores and cracks.

Comparison with experimental data shows a good agreement for the P-wave. Moreover, applying this model to published data indicates that the estimated pore geometry depends on the choice of the theoretical approach, and that there are variations of the crack radius and aperture with pressure. We also show that it is possible to obtain the rock permeability based on the estimated pore geometry. The model provides the possibility to quantify the effect of multiscale cracks on broadband wave velocity dispersion with respect to pressure, and predict the transport properties.

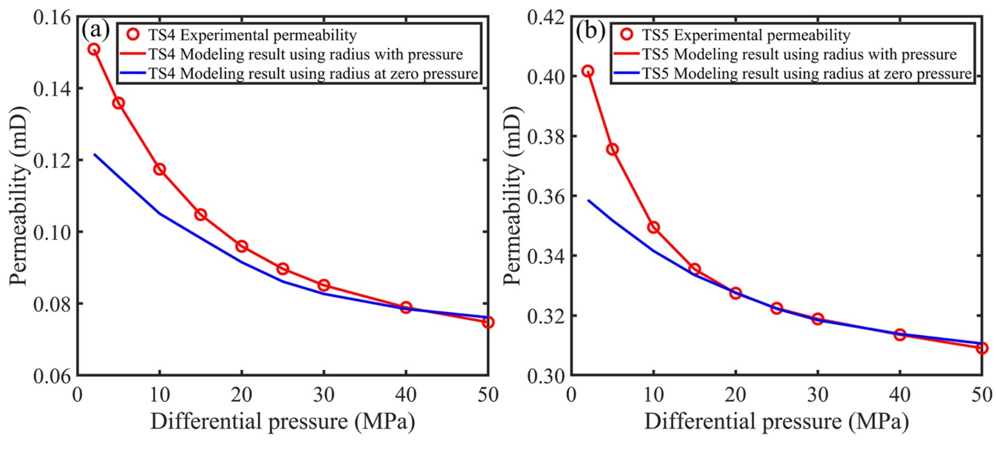

Figure 14. Comparison of the measured and theoretical permeabilities versus differential pressure for samples TS4 (a) and TS5 (b). The theory is based on Equations 18 and 19 by assuming variations of the pore/crack radii with pressure (red curve) and constant radii (blue curve).

10.1029/2023JB027474

Data Availability Statement

The experimental data of two tight sandstones can be downloaded at http://dx.doi.org/10.17632/m2brb3dw2g.1 (Ba et al., 2023). The measurements of a tight sandstone and a low-porosity sandstone can be found in Yin et al. (2017) (https://doi.org/10.1002/2017JB014244) and Li et al. (2022) (https://doi.org/10.6038/cjg2022P0473).

Acknowledgments
This work is funded by the National Natural Science Foundation of China (42104110, 41974123, and 42174161), the Natural Science Foundation of Jiangsu Province (BK20210379 and BK20200021), and the China Postdoctoral Science Foundation (2022M720989).

References

Akamatsu, Y., Nagase, K., Abe, N., Okazaki, K., Hatakeyama, K., & Katayama, I. (2023). Cross-property relationship between electrical resistivity and elastic wave velocity of crustal rocks from the Oman Drilling Project Hole GT3A: Implications for in situ geophysical properties of oceanic crust. *Journal of Geophysical Research: Solid Earth*, *128*(6), e2022JB026130. https://doi.org/10.1029/2022jb026130

Al-Wardy, W., & Zimmerman, R. W. (2004). Effective stress law for the permeability of clay-rich sandstones. *Journal of Geophysical Research: Solid Earth*, *109*(B4), B04203. https://doi.org/10.1029/2003JB002836

Amalokwu, K., & Falcon-Suarez, I. H. (2021). Effective medium modeling of pressure effects on the joint elastic and electrical properties of sandstones. *Journal of Petroleum Science and Engineering*, *202*, 108540. https://doi.org/10.1016/j.petrol.2021.108540

Arena, A., Delle Piane, C., & Sarout, J. (2014). A new computational approach to cracks quantification from 2D image analysis: Application to micro-cracks description in rocks. *Computers & Geosciences*, *66*, 106–120. https://doi.org/10.1016/j.cageo.2014.01.007

Ba, J., Carcione, J. M., & Nie, J. X. (2011). Biot-Rayleigh theory of wave propagation in double-porosity media. *Journal of Geophysical Research: Solid Earth*, *116*(B6), B06202. https://doi.org/10.1029/2010JB008185

Ba, J., Xu, W., Fu, L. Y., Carcione, J. M., & Zhang, L. (2017). Rock anelasticity due to patchy saturation and fabric heterogeneity: A double double-porosity model of wave propagation. *Journal of Geophysical Research: Solid Earth*, *122*(3), 1949–1976. https://doi.org/10.1002/2016JB013882

Ba, J., Zhang, L., Zhu, H. S., & Carcione, J. M. (2023). Effect of multi-scale cracks on seismic waves propagating in tight sandstones [Dataset]. Mendeley Data, V1. https://doi.org/10.17632/m2brb3dw2g.1

Borgomano, J. V., Pimienta, L. X., Fortin, J., & Guéguen, Y. (2019). Seismic dispersion and attenuation in fluid-saturated carbonate rocks: Effect of microstructure and pressure. *Journal of Geophysical Research: Solid Earth*, *124*(12), 12498–12522. https://doi.org/10.1029/2019JB018434

Burns, D. R., Cheng, C. H., & Wilkens, R. H. (1985). *Sandstone pore aspect ratio spectra from direct observations and velocity inversion*. Massachusetts Institute of Technology, Earth Resources Laboratory. Retrieved from http://hdl.handle.net/1721.1/75073

Carcione, J. M. (2022). *Wave Fields in Real Media. Theory and numerical simulation of wave propagation in anisotropic, anelastic, porous and electromagnetic media*. Elsevier. (Fourth edition, extended and revised).

Carcione, J. M., & Picotti, S. (2006). P-wave seismic attenuation by slow-wave diffusion: Effects of inhomogeneous rock properties. *Geophysics*, *71*(3), O1–O8. https://doi.org/10.1190/1.2194512

Chapman, M., Zatsepin, S. V., & Crampin, S. (2002). Derivation of a microstructural poroelastic model. *Geophysical Journal International*, *151*(2), 427–451. https://doi.org/10.1046/j.1365-246X.2002.01769.x

Cheng, C. H. (1978). Seismic velocities in porous rocks—Direct and inverse problems (ScD thesis). Massachusetts Institute of Technology.

Cheng, C. H., & Toksöz, M. N. (1979). Inversion of seismic velocities for the pore aspect ratio spectrum of a rock. *Journal of Geophysical Research: Solid Earth*, *84*(B13), 7533–7543. https://doi.org/10.1029/JB084iB13p07533

Clark, V. A., Tittmann, B. R., & Spencer, T. W. (1980). Effect of volatiles on attenuation (Q-1) and velocity in sedimentary rocks. *Journal of Geophysical Research: Solid Earth*, *85*(B10), 5190–5198. https://doi.org/10.1029/JB085iB10p05190

David, E. C., & Zimmerman, R. W. (2012). Pore structure model for elastic wave velocities in fluid-saturated sandstones. *Journal of Geophysical Research: Solid Earth*, *117*(B7), B07210. https://doi.org/10.1029/2012JB009195

Deng, J. X., Zhou, H., Wang, H., Zhao, J. G., & Wang, S. X. (2015). The influence of pore structure in reservoir sandstone on dispersion properties of elastic waves. *Chinese Journal of Geophysics-Chinese Edition*, *58*(9), 3389–3400. https://doi.org/10.6038/cjg2015093

Duan, C., Deng, J., Li, Y., Lu, Y., Tang, Z., & Wang, X. (2018). Effect of pore structure on the dispersion and attenuation of fluid-saturated tight sandstone. *Journal of Geophysics and Engineering*, *15*(2), 449–460. https://doi.org/10.1088/1742-2140/aa8b82

Dvorkin, J., Mavko, G., & Nur, A. (1995). Squirt flow in fully saturated rocks. *Geophysics*, *60*(1), 97–107. https://doi.org/10.1190/1.1443767

Dvorkin, J., & Nur, A. (1993). Dynamic poroelasticity: A unified model with the squirt and the Biot mechanisms. *Geophysics*, *58*(4), 524–533. https://doi.org/10.1190/1.1443435

Gassmann, F. (1951). Über die elastizität poröser medien: Vier. der Natur. *Gesellschaft Zürich*, *96*, 1–23.

Griffiths, L., Heap, M. J., Baud, P., & Schmittbuhl, J. (2017). Quantification of microcrack characteristics and implications for stiffness and strength of granite. *International Journal of Rock Mechanics and Mining Sciences*, *100*, 138–150. https://doi.org/10.1016/j.ijrmms.2017.10.013

Guéguen, Y., & Kachanov, M. (2011). Effective elastic properties of cracked rocks—An overview. In Y. M. Leroy & F. K. Lehner (Eds.), *Mechanics of crustal rocks* (pp. 73–125). Springer. https://doi.org/10.1007/978-3-7091-0939-7_3

Guo, J., & Gurevich, B. (2020). Frequency-dependent P wave anisotropy due to wave-induced fluid flow and elastic scattering in a fluid-saturated porous medium with aligned fractures. *Journal of Geophysical Research: Solid Earth*, *125*(8), e2020JB020320. https://doi.org/10.1029/2020JB020320

Guo, J., Gurevich, B., & Chen, X. (2022). Dynamic SV-wave signatures of fluid-saturated porous rocks containing intersecting fractures. *Journal of Geophysical Research: Solid Earth*, *127*(8), e2022JB024745. https://doi.org/10.1029/2022JB024745

Guo, J., Zhao, L., Chen, X., Yang, Z., Li, H., & Liu, C. (2022). Theoretical modelling of seismic dispersion, attenuation and frequency-dependent anisotropy in a fluid-saturated porous rock with intersecting fractures. *Geophysical Journal International*, *230*(1), 580–606. https://doi.org/10.1093/gji/ggac070

Gurevich, B., & Carcione, J. M. (2022). Attenuation and dispersion of elastic waves in porous rocks: Mechanisms and models. https://doi.org/10.1190/1.9781560803911

Gurevich, B., Makarynska, D., de Paula, O. B., & Pervukhina, M. (2010). A simple model for squirt-flow dispersion and attenuation in fluid-saturated granular rocks. *Geophysics*, *75*(6), N109–N120. https://doi.org/10.1190/1.3509782

Hadley, K. (1976). Comparison of calculated and observed crack densities and seismic velocities in Westerly granite. *Journal of Geophysical Research: Solid Earth*, *81*(20), 3484–3494. https://doi.org/10.1029/JB081i020p03484

Han, T. (2016). A simple way to model the pressure dependency of rock velocity. *Tectonophysics*, *675*, 1–6. https://doi.org/10.1016/j.tecto.2016.03.008

Han, T., Clennell, M. B., Cheng, A. C., & Pervukhina, M. (2016). Are self-consistent models capable of jointly modeling elastic velocity and electrical conductivity of reservoir sandstones? *Geophysics*, *81*(4), D377–D382. https://doi.org/10.1190/geo2015-0690.1

Ingber, L. (1993). Simulated annealing: Practice versus theory. *Mathematical and Computer Modelling*, *18*(11), 29–57. https://doi.org/10.1016/0895-7177(93)90204-C

Izumotani, S., & Onozuka, S. (2013). Elastic moduli and the aspect ratio spectrum of rock using simulated annealing. *Geophysical Prospecting*, *61*(s1), 489–504. https://doi.org/10.1111/1365-2478.12003

Kuteynikova, M., Tisato, N., Jänicke, R., & Quintal, B. (2014). Numerical modeling and laboratory measurements of seismic attenuation in partially saturated rock. *Geophysics*, *79*(2), L13–L20. https://doi.org/10.1190/geo2013-0020.1

Li, Z., Ouyang, F., Xiao, Z., Liu, X., He, Y., & Zhao, J. (2022). Experimental and theoretical verification of the effect of fluid viscosity on the dispersion and decay of sandstone elastic modulus [Dataset]. *Chinese Journal of Geophysics*, *65*(6), 2179–2197. https://doi.org/10.6038/cjg2022P0473

Mavko, G., & Jizba, D. (1991). Estimating grain-scale fluid effects on velocity dispersion in rocks. *Geophysics*, *56*(12), 1940–1949. https://doi.org/10.1190/1.1443005

Mavko, G., & Nur, A. (1975). Melt squirt in the asthenosphere. *Journal of Geophysical Research: Solid Earth*, *80*(11), 1444–1448. https://doi.org/10.1029/JB080i011p01444

Müller, T. M., Gurevich, B., & Lebedev, M. (2010). Seismic wave attenuation and dispersion resulting from wave-induced flow in porous rocks—A review. *Geophysics*, *75*(5), 75A147–75A164. https://doi.org/10.1190/1.3463417

Norris, A. N. (1985). A differential scheme for the effective moduli of composites. *Mechanics of Materials*, *4*(1), 1–16. https://doi.org/10.1016/0167-6636(85)90002-X

O'Connell, R. J., & Budiansky, B. (1977). Viscoelastic properties of fluid-saturated cracked solids. *Journal of Geophysical Research: Solid Earth*, *82*(36), 5719–5735. https://doi.org/10.1029/JB082i036p05719

Ouyang, F., Zhao, J., Li, Z., Xiao, Z., He, Y., Deng, J., et al. (2021). Modeling velocity dispersion and attenuation using pore structure characteristics of rock. *Chinese Journal of Geophysics-Chinese Edition*, *64*(3), 1034–1047. https://doi.org/10.6038/cjg2021O0355

Peng, S., & Johnson, A. M. (1972). Crack growth and faulting in cylindrical specimens of Chelmsford granite. *International Journal of rock Mechanics & Mining Sciences*, *9*(1), 37–86. https://doi.org/10.1016/0148-9062(72)90050-2

Pimienta, L., Fortin, J., & Guéguen, Y. (2014). Investigation of elastic weakening in limestone and sandstone samples from moisture adsorption. *Geophysical Journal International*, *199*(1), 335–347. https://doi.org/10.1093/gji/ggu257

Pride, S. R., Berryman, J. G., & Harris, J. M. (2004). Seismic attenuation due to wave-induced flow. *Journal of Geophysical Research: Solid Earth*, *109*(B1), B01201. https://doi.org/10.1029/2003JB002639

Qin, X., Han, D.-H., & Zhao, L. (2022). Measurement of grain bulk modulus on sandstone samples from the Norwegian Continental Shelf. *Journal of Geophysical Research: Solid Earth*, *127*(9), e2022JB024550. https://doi.org/10.1029/2022JB0245

Quintal, B., Steeb, H., Frehner, M., Schmalholz, S. M., & Saenger, E. H. (2012). Pore fluid effects on S-wave attenuation caused by wave-induced fluid flow. *Geophysics*, *77*(3), L13–L23. https://doi.org/10.1190/geo2011-0233.1

Raymond, J., Comeau, F. A., Malo, M., Blessent, D., & Sánchez, I. L. (2017). The Geothermal Open Laboratory: A free space to measure thermal and hydraulic properties of geological materials. In *IGCP636 annual meeting* (Vol. 2017).

Sarout, J. (2012). Impact of pore space topology on permeability, cut-off frequencies and validity of wave propagation theories. *Geophysical Journal International*, *189*(1), 481–492. https://doi.org/10.1111/j.1365-246X.2011.05329.x

Sarout, J., Cazes, E., Delle Piane, C., Arena, A., & Esteban, L. (2017). Stress-dependent permeability and wave dispersion in tight cracked rocks: Experimental validation of simple effective medium models. *Journal of Geophysical Research: Solid Earth*, *122*(8), 6180–6201. https://doi.org/10.1002/2017JB014147

Shapiro, S. A. (2003). Elastic piezosensitivity of porous and fractured rocks. *Geophysics*, *68*(2), 482–486. https://doi.org/10.1190/1.1567215

Shapiro, S. A., Khizhniak, G. P., Plotnikov, V. V., Niemann, R., Ilyushin, P. Y., & Galkin, S. V. (2015). Permeability dependency on stiff and compliant porosities: A model and some experimental examples. *Journal of Geophysics and Engineering*, *12*(3), 376–385. https://doi.org/10.1088/1742-2132/12/3/376

Sprunt, E. S., & Brace, W. F. (1974). Direct observation of microcavities in crystalline rocks. *International Journal of rock Mechanics & Mining Sciences*, *11*(4), 139–150. https://doi.org/10.1016/0148-9062(74)92874-5

Sun, C., Fortin, J., Borgomano, J. V., Wang, S., Tang, G., Bultreys, T., & Cnudde, V. (2022). Influence of fluid distribution on seismic dispersion and attenuation in partially saturated limestone. *Journal of Geophysical Research: Solid Earth*, *127*(5), e2021JB023867. https://doi.org/10.1029/2021JB023867

Sun, Y., & Gurevich, B. (2020). Modeling the effect of pressure on the moduli dispersion in fluid-saturated rocks. *Journal of Geophysical Research: Solid Earth*, *125*(8), e2019JB019297. https://doi.org/10.1029/2019JB019297

Tang, X. M. (2011). A unified theory for elastic wave propagation through porous media containing cracks—An extension of Biot's poroelastic wave theory. *Science China Earth Sciences*, *54*(9), 1441–1452. https://doi.org/10.1007/s11430-011-4245-7

Tang, X. M., Chen, X. L., & Xu, X. K. (2012). A cracked porous medium elastic wave theory and its application to interpreting acoustic data from tight formations. *Geophysics*, *77*(6), D245–D252. https://doi.org/10.1190/geo2012-0091.1

Tang, X. M., Wang, H., Su, Y., & Chen, X. (2021). Inversion for micro-pore structure distribution characteristics using cracked porous medium elastic wave theory. *Chinese Journal of Geophysics-Chinese Edition*, *64*(8), 2941–2951. https://doi.org/10.6038/cjg2021O0478

Thomsen, L. (1985). Biot-consistent elastic moduli of porous rocks: Low-frequency limit. *Geophysics*, *50*(12), 2797–2807. https://doi.org/10.1190/1.1441900

Toksöz, M. N., Cheng, C. H., & Timur, A. (1976). Velocities of seismic waves in porous rocks. *Geophysics*, *41*(4), 621–645. https://doi.org/10.1111/j.1365-2478.1993.tb00578.x

Tran, D. T., Rai, C. S., & Sondergeld, C. H. (2008). Changes in crack aspect-ratio concentration from heat treatment: A comparison between velocity inversion and experimental data. *Geophysics*, *73*(4), E123–E132. https://doi.org/10.1190/1.2928848

Walsh, J. B. (1965). The effect of cracks on the compressibility of rock. *Journal of Geophysical Research*, *70*(2), 381–389. https://doi.org/10.1029/JZ070i002p00381

Wang, H. M., & Tang, X. M. (2021). Inversion of dry and saturated P-and S-wave velocities for the pore-aspect-ratio spectrum using a cracked porous medium elastic wave theory. *Geophysics*, *86*(6), A57–A62. https://doi.org/10.1190/geo2021-0071.1

Wawersik, W. R., & Brace, W. F. (1971). Post-failure behavior of a granite and diabase. *Rock Mechanics*, *3*(2), 61–85. https://doi.org/10.1007/BF01239627

Wei, Q., Wang, Y., Han, D. H., Sun, M., & Huang, Q. (2021). Combined effects of permeability and fluid saturation on seismic wave dispersion and attenuation in partially-saturated sandstone. *Advanced in Geo-Energy Research*, *5*(2), 181–190. https://doi.org/10.46690/ager.2021.02.07

Wu, C. F., Ba, J., Carcione, J. M., Müller, T. M., & Zhang, L. (2022). A patchy-saturated rock physics model for tight sandstone based on microscopic pore structures. *Applied Geophysics*, *19*(2), 147–160. https://doi.org/10.1007/s11770-022-0938-2

Yan, F., Han, D. H., Yao, Q., & Zhao, L. (2014). Prediction of seismic wave dispersion and attenuation from ultrasonic velocity measurements. *Geophysics*, *79*(5), WB1–WB8. https://doi.org/10.1190/geo2013-0416.1

Yao, Q., Han, D. H., Yan, F., & Zhao, L. (2015). Modeling attenuation and dispersion in porous heterogeneous rocks with dynamic fluid modulus. *Geophysics*, *80*(3), D183–D194. https://doi.org/10.1190/geo2013-0410.1

Yin, H., Borgomano, J. V., Wang, S., Tiennot, M., Fortin, J., & Guéguen, Y. (2019). Fluid substitution and shear weakening in clay-bearing sandstone at seismic frequencies. *Journal of Geophysical Research: Solid Earth*, *124*(2), 1254–1272. https://doi.org/10.1029/2018JB016241

Yin, H., Zhao, J., Tang, G., Zhao, L., Ma, X., & Wang, S. (2017). Pressure and fluid effect on frequency-dependent elastic moduli in fully saturated tight sandstone [Dataset]. Journal of Geophysical Research: Solid Earth, *122*(11), 8925–8942. https://doi.org/10.1002/2017JB014244

Zhang, L., Ba, J., & Carcione, J. M. (2021). Wave propagation in infinituple-porosity media. *International Journal of Rock Mechanics and Mining Sciences*, *126*(4), e2020JB021266. https://doi.org/10.1029/2020JB021266

Zhang, L., Ba, J., Carcione, J. M., & Fu, L. Y. (2020). Differential poroelasticity model for wave dissipation in self-similar rocks. *International Journal of Rock Mechanics and Mining Sciences*, *128*, 104281. https://doi.org/10.1016/j.ijrmms.2020.104281

Zhang, L., Ba, J., Carcione, J. M., & Sun, W. (2019). Modeling wave propagation in cracked porous media with penny-shaped inclusions. *Geophysics*, *84*(4), WA141–WA151. https://doi.org/10.1190/geo2018-0487.1

Zhang, L., Ba, J., Fu, L., Carcione, J. M., & Cao, C. (2019). Estimation of pore microstructure by using the static and dynamic moduli. *International Journal of Rock Mechanics and Mining Sciences*, *113*, 24–30. https://doi.org/10.1016/j.ijrmms.2018.11.005

Zhang, L., Ba, J., Li, C., Carcione, J. M., & Zhou, F. (2022). Joint inversion of the unified pore geometry of tight sandstones based on elastic and electrical properties. *Journal of Petroleum Science and Engineering*, *219*, 111109. https://doi.org/10.1016/j.petrol.2022.111109

Zhang, Y., & Toksöz, M. N. (2012). Impact of the cracks lost in the imaging process on computing linear elastic properties from 3D microtomographic images of Berea sandstone. *Geophysics*, *77*(2), R95–R104. https://doi.org/10.1190/geo2011-0126.1

Zhao, L., Tang, G., Wang, S., Zhao, J., Wang, X., Liu, H., et al. (2019). Laboratory study of oil saturation and oil/water substitution effects on a sandstone's modulus dispersion and attenuation. *Exploration Geophysics*, *50*(3), 324–335. https://doi.org/10.1080/08123985.2019.1610327

Zimmerman, R. W. (1990). *Compressibility of sandstones*. Elsevier.